Constraining the nature of the most extreme Galactic particle accelerator. H.E.S.S. observations of the microquasar V4641 Sgr

```
A. Acharyya¹o, F. Aharonian²³o, H. Ashkar⁴o, M. Backes⁵,6o, R. Batzofin³o, D. Berge³,9o, K. Bernlöhr³o, M. Böttcher6o, C. Boisson¹o, J. Bolmont¹¹o, F. Brun¹²o, B. Bruno¹³, C. Burger-Scheidlin²o, T. Bylund¹o, S. Casanova¹⁴o, J. Celic¹³, M. Cerruti¹⁵o, A. Chen¹6o, M. Chernyakova¹¹².²o, J. O. Chibueze6₀5o, O. Chibueze6₀ B. Cornejo¹²o, G. Cotter¹³o, J. de Assis Scarpin⁴o, M. de Bony de Lavergne¹².¹¹oo, M. de Naurois⁴o, E. de Oña Wilhelmi³o, A. G. Delgado Giler³o, J. Devin²oo, A. Djannati-Ataï¹⁵o, A. Dmytriiev6o, K. Egberts³o, K. Egg¹³o, J.-P. Ernenwein¹o, C. Escañuela Nieves³o, P. Fauverge²¹o, K. Feijen¹⁵o, M. D. Filipovic²²o, G. Fontaine⁴o, S. Funk¹³o, S. Gabici¹⁵, Y.A. Gallant²o, J.F. Glicenstein¹²o, J. Glombitza¹³o, P. Goswami²³o, M.-H. Grondin²¹o, L. Heckmann¹⁵o, B. Heβ²⁴o, J.A. Hinton³o, W. Hofmann³o, T. L. Holch⁵o, M. Holler²o, M. Jamrozy²oo, F. Jankowsky²³, A. Jardin-Blicq²¹o, I. Jaroschewski¹²o, D. Jimeno⁵o, I. Jung-Richard¹³, K. Katarzyński²³o, D. Kerszberg¹¹o, B. Khélifi¹ō, N. Komin²o¹oo, K. Kosack¹²o, D. Kostunin⁵o, R.G. Lang¹³o, S. Lazarević²²o, A. Lemière¹⁵, M. Lemoine-Goumard²¹o, J.-P. Lenain¹¹o, P. Liniewicz²oo, A. Luashvilioo, J. Mackey²o, D. Malyshev²oo, V. Marandon¹²o, M. G. F. Mayer¹³o, A. Mehta⁵o, A. M.W. Mitchell¹³o, R. Moderski²oo, L. Mohrmann³o, A. Montanari²aoo, E. Moulin¹²oo, J. Niemiec¹⁴o, L. Olivera-Nieto³oo, A. Quirrenbach²oo, S. Panny²oo, R.D. Parsonsooo, U. Pensec¹¹oo, P. Pichard¹⁵oo, T. Preis²ōo, G. Pühlhofer²⁴oo, M. Punch¹⁵oo, A. Quirrenbach²oo, A. Reimer²oo, O. Reimer²oo, I. Reis¹²oo, V. Sahakian³oo, A. Santangelo²⁴oo, M. Sasaki¹³oo, F. Schüssler¹²oo, J.N.S. Shapopi⁵oo, W. Si Said⁴oo, H. Sol¹oo, N. Tsuji³⁴oo, S. Safi-Harb³ooo, V. Sahakian³oo, A. M. Taylor³oo, C. Venter6oo, J. Vink²oo, V. Voitsekhovskyi²oo, S.J. Wagner²oo, A. Wierzcholska¹⁴oo, M. Zacharias²ooo, A.A. Zdziarski²oo, A. Zech¹oo, W. Zhong⁵oo (H.E.S.S. Collaboration).
```

S. Takekawa³⁶

(Affiliations can be found after the references)

Received 3 October 2025 / Accepted 6 November 2025

ABSTRACT

Context. Microquasars have emerged as promising candidates to explain the cosmic-ray flux at petaelectronvolt energies. LHAASO observations revealed V4641 Sgr as the most extreme example so far. Its gamma-ray spectrum extends up to 800 TeV, which requires particles with multi-PeV energy. The TeV emission is highly extended, which challenges expectations given the reported low-inclination angle of the V4641 Sgr jets.

Aims. We spatially and spectrally resolved the gamma-ray emission from V4641 Sgr and investigated the particle acceleration in the system.

Methods. Using \$\times 100\$ h of H.E.S.S. data, we performed a spectro-morphological study of the gamma-ray emission around V4641 Sgr. We

Methods. Using ≈ 100 h of H.E.S.S. data, we performed a spectro-morphological study of the gamma-ray emission around V4641 Sgr. We employed HI and dedicated CO observations of the region to infer the target material for cosmic-ray interactions.

Results. We detected multi-TeV emission around V4641 Sgr with a high significance. The emission region is elongated, and its major and minor axes are $0.34^{\circ}_{\pm 0.01_{syst}}^{\pm 0.04_{stat}}$ and $0.06^{\circ}_{\pm 0.01_{syst}}^{\pm 0.01_{syst}}$, respectively. We found a power-law spectrum with an index ≈ 1.8 , and together with results from other gamma-ray instruments, this reveals a spectral energy distribution (SED) that peaks at energies of ≈ 100 TeV for the first time. We found indications (3 σ) of a two-component morphology, with indistinguishable spectral properties. The position of V4641 Sgr is inconsistent with the best-fit position of the single-component model and with the dip between the two components. We found no significant evidence of an energy-dependent morphology. No dense gas was found at any distance towards V4641 Sgr, which places an upper limit of $n_{gas} \lesssim 0.2$ cm⁻³ within the gamma-ray emission region.

Conclusions. The peak of the SED at ≈ 100 TeV identifies V4641 Sgr as a candidate cosmic-ray accelerator beyond the so-called knee. The absence of dense target gas places stringent energetic constraints on hadronic interpretations, however. The H.E.S.S. measurement requires an unusually hard (≈ 1.5) spectral index for the protons. A leptonic scenario faces fewer obstacles if the particle transport is fast enough to avoid losses and to reproduce the observed energy-independent morphology. The absence of bright X-ray emission across the gamma-ray emission region requires a magnetic field strength $\lesssim 3~\mu\text{G}$, however. Our findings favour a leptonic origin of the gamma-ray emission. This conclusion does not exclude hadron acceleration in the V4641 Sgr system.

Key words. Acceleration of particles – Radiation mechanisms: non-thermal – Gamma rays: stars – Stars: binaries – Stars: jets

1. Introduction

The origin of the cosmic-ray spectrum measured at Earth remains one of the largest mysteries in high-energy astrophysics. Precise measurements have revealed several spectral features that were interpreted as a result of differences in the production processes or astrophysical source classes involved, and also

Send offprint requests to:

e-mail: contact.hess@hess-experiment.eu;

cosmic-ray propagation through space. At energies of a few petaelectronvolts, a spectral break (usually referred to as the knee) was measured (Amenomori et al. 2008; Aartsen et al. 2019; LHAASO Collaboration et al. 2025). Below this energy, convincing theoretical arguments and experimental evidence have suggested that particles are predominantly accelerated in supernova remnants (SNRs, see e.g. Ginzburg & Syrovatskii 1964; Hillas 2005; Bell 2014). Because cosmic rays arriving at Earth have undergone multiple scatterings in the turbulent magnetic field of the Galaxy, astrophysical sources of high-energy parti-

^{*} Corresponding authors

cles are better studied through neutral secondaries produced via interactions of particles with their source environment: photons and neutrinos. Gamma-ray observations in the TeV domain have identified hundreds of sources with a wide variety of types, including SNRs. The observed gamma-ray spectra of SNRs show cut-offs in energy at a few dozen TeV, however, corresponding to sub-PeV primary particles (e.g. H.E.S.S. Collaboration et al. 2018b; Abeysekara et al. 2020). Even higher gamma-ray energies have only become accessible in recent years, but observations have yet to reveal an SNR source whose emission extends to the required energies to account for the knee feature (Cao et al. 2024).

As a consequence, other source classes have increasingly been considered as accelerators of the highest-energy Galactic cosmic rays. One such class of objects are microquasars. These are stellar binary systems hosting a neutron star or a black hole (X-ray binaries) and launch powerful and often relativistic jets. Microquasar jets have long been proposed as sites for acceleration to TeV and PeV energies (e.g. Aharonian 2004; Bosch-Ramon et al. 2005a; Cooper et al. 2020; Kantzas et al. 2023), and experimental evidence supporting these claims has increased recently. In particular, the first report of TeV emission from a microquasar (SS 433) by the High-Altitude Water Cherenkov (HAWC) Observatory (Abeysekara et al. 2018) and the follow-up high-resolution study with the High Energy Stereoscopic System (H.E.S.S., H.E.S.S. Collaboration et al. 2024) revealed efficient particle acceleration sites in the jets at a distance of some dozen parsecs (pc) from the central binary. A second TeV detection of a microquasar (V4641 Sgr) was reported by the HAWC Collaboration (Alfaro et al. 2024), which prompted follow-up observations with H.E.S.S. The result of these observations is reported in this paper. The Large High Altitude Air Shower Observatory (LHAASO) recently reported the detection of gamma-rays with energies > 25 TeV from these two systems and three additional accreting black-hole binary systems (LHAASO Collaboration 2024b). In particular, the LHAASO spectrum of V4641 Sgr extends to 800 TeV at least, which means that particle acceleration to multi-PeV energies is required in the system.

Among other PeV accelerator candidates, V4641 Sgr stands out as an ideal laboratory for the study of cosmic-ray acceleration. Unlike many of the sources detected by LHAASO above some hundred TeV, V4641 Sgr lies several degrees off the Galactic plane and not in a crowded star-forming region (LHAASO Collaboration 2024a). Accordingly, the identification of the microquasar as the counterpart of the gammaray source is firm. Additionally, protons and other nuclei are known to be present in microquasar jets (Margon et al. 1979; Díaz Trigo et al. 2013). Specifically, emission lines from iron and other metals have been attributed to the jets of V4641 Sgr (in't Zand et al. 2000). Regardless of whether the observed ultra-high-energy photons originate from inverse-Compton (IC) scattering of PeV electrons, or from neutral-pion decay following inelastic collisions of multi-PeV nuclei with ambient gas, the idea that these sources contribute to the local cosmic-ray spectrum above PeV energies remains compelling.

We present the H.E.S.S. view of V4641 Sgr. H.E.S.S. is an array of imaging atmospheric Cherenkov telescopes (IACTs) that provides a superior angular and spectral resolution compared to the HAWC and LHAASO arrays of water Cherenkov detectors (WCDs) (e.g. Hinton & Hofmann 2009). This enables a detailed study of the gamma-ray emission properties of V4641 Sgr.

The paper is organised as follows. In Section 2 we introduce the microquasar V4641 Sgr and summarise the knowledge about the system. We then describe the H.E.S.S. telescopes and the procedure we used to select and analyse the data in Section 3. We report the results of the spectral and morphological characterisation of the emission in Section 4 and on the dedicated radio observations in Section 5. These are combined with insights from previous multi-wavelength observations to discuss the physical implications in Section 6. Finally, our conclusions are collected in Section 7.

2. The microquasar V4641 Sgr

V4641 Sgr (SAX J1819.3–2525, XTE J1819–254), located at Galactic coordinates l=6.7740° and b=-4.7891°, is a low-mass Galactic X-ray binary (LMXB) system with a period of 2.81728 days (Goranskij 2001; Orosz et al. 2001). It was identified as such in 1999, when it underwent a strong outburst (Markwardt et al. 1999; in't Zand et al. 2000; Wijnands & van der Klis 2000) during which its X-ray luminosity increased by several orders of magnitude. Modelling of the binary orbit yielded an estimate for the mass of the compact object in V4641 Sgr of $M_{BH} \approx 7 M_{\odot}$ (Goranskij et al. 2003; Orosz et al. 2001; MacDonald et al. 2014), which firmly identified it as a black hole. The companion star mass is estimated to be $M_* \approx 3 M_{\odot}$, making it one of the most massive companions observed in a LMXB system. The mass of the companion constrains the system age to < 1 Gyr (Salvesen & Pokawanvit 2020).

During the X-ray outburst in 1999, radio observations revealed an extended, fast-changing radio source typical of relativistic outflows (Hjellming et al. 2000). The proper motions of the radio source were claimed to be (apparently) superluminal (Hjellming et al. 2000), which has been interpreted as evidence for the existence of a relativistic jet propagating with a low inclination angle with respect to our line of sight (Orosz et al. 2001; Salvesen & Pokawanvit 2020). However, Hjellming et al. (2000) did not directly observe fast proper motions: they were inferred under the assumption that the radio blobs were launched at the same time as the X-ray outburst.

Additional X-ray observations of the same outburst revealed the presence of bright, relativistic iron lines (in't Zand et al. 2000; Miller et al. 2002) in addition to an unusually broad emission feature in the X-ray spectrum above 4 keV. This feature has been interpreted as a blend of Doppler-shifted Fe lines, much like in the jets of SS 433 (Marshall et al. 2002), or alternatively similar to the spectra of blazars at the onset of an inverse Compton hump (Gallo et al. 2014). Both interpretations require the axis of the jets to be closely aligned with our line of sight, consistent with the interpretation of the radio observations. Optical (Revnivtsev et al. 2002a) and X-ray (Revnivtsev et al. 2002b) observations during the 1999 outburst suggest the presence of an extended envelope obscuring the source, which required mass accretion rates during the outburst exceeding the Eddington limit of $\dot{M}c^2 > L_{\rm Edd} = 1.26 \times 10^{38} \, (M_{\rm BH}/M_{\odot})$ erg s⁻¹ $\approx 10^{39}$ erg s⁻¹.

While the claim of super-luminal motion would suggest a jetted source that points towards us, studies of the inclination of the orbital plane provide contradictory results, or at least imply that the jet is not perpendicular to the orbital plane. Modelling of the binary orbit suggests that the orbital plane has an inclination $i_{\rm orb} = 72.3 \pm 4.1^{\circ}$ (Orosz et al. 2001; MacDonald et al. 2014), which has been cited as evidence of precession (e.g. Gallo et al. 2014). Such a large misalignment with the jet inclination inferred from the observation of apparent super-luminal motions

 $(i_{\rm jet} < 16^\circ)$ cannot be explained via a natal kick from the progenitor supernova event (Salvesen & Pokawanvit 2020). Additionally, estimates of the inclination of the inner accretion disk yield a relatively high value of $i_{\rm disk} = 43 \pm 15^\circ$ (Miller et al. 2002). Martin et al. (2008) considered the possibility that these mismatches could be explained by a warped accretion disk, though concluded that this is not a viable explanation and that the observed $i_{\rm disk}$ and $i_{\rm jet}$ are in tension. Unfortunately, despite subsequent less powerful radio and X-ray flares (e.g. Muñoz-Darias et al. 2018; Shaw et al. 2022), there have been no further direct detections of the jet since the 1999 outburst, and thus uncertainty about the geometry of the system remains.

The constraints on the distance of the binary system are less ambiguous. While Hjellming et al. (2000) assumed a modest distance of 0.5 kpc, the earliest quantitative estimate of the distance to V4641 Sgr was made by Orosz et al. (2001) by determining the spectral type of the companion star during X-ray quiescence and comparing it to the observed magnitude accounting for extinction, finding $d = 9.6 \pm 2.5$ kpc. This calculation was updated by MacDonald et al. (2014), which accounted for optical variability during the X-ray quiescence period and yielded $d = 6.2 \pm 0.7$ kpc. Measurements of parallax with the Gaia satellite (Bailer-Jones et al. 2018) provide an independent distance estimate. A dedicated analysis of the Gaia data, taking into account the proper motion of the binary (Gandhi et al. 2019), yields a consistent estimate of $d = 6.62 \pm 1.81$ kpc. For simplicity we will adopt d = 6.2 kpc throughout this work, unless specified otherwise. The distance could however plausibly lie somewhere between 5 and 8 kpc.

The identification of V4641 Sgr as a gamma-ray source was reported by the HAWC collaboration, who detected an extended source around the microquasar (Alfaro et al. 2024). Due to its location below the Galactic plane, it is unlikely that another unknown Galactic counterpart could account for the observed gamma rays. Analysis of the HAWC source revealed that the best-fit morphological model is one extended ($\sigma_{\text{major}} = 0.54 \pm$ $0.08\pm0.1^{\circ}$, which de-projected corresponds to $58.4d_{6.2\mathrm{kpc}}$ pc) and highly elliptical ($e = 0.98 \pm 0.01$) component with a power-law spectrum of index 2.1 ± 0.1 (Alfaro et al. 2024). A model with two point sources at distances of 0.23° and 0.46° from the binary was also considered, but could not be statistically distinguished from the single extended model. Measurements by LHAASO reveal a source with consistent morphology whose spectrum reaches up to at least 800 TeV (LHAASO Collaboration 2024b), firmly ruling out an extragalactic origin. In the GeV band, Zhao et al. (2025) analysed 15 years of data from the Fermi Large Area Telescope (LAT) and reported no detected emission across the entire region, neither steady nor variable. They derive upper limits using a spatial template constructed with the LHAASO significance map, which suffers from being convolved with the LHAASO angular resolution of tens of arcmin.

It is not understood why a jet of reported low angle with our line of sight would produce such extended and asymmetric gamma-ray emission, measuring over 100 pc across when projected onto the sky. One possible explanation could be the proper motion of the source. However, the direction of the proper motion of V4641 Sgr does not align with the orientation of the observed gamma-ray emission, but is instead orientated directly upwards towards the Galactic plane (see Figure 3 in Gandhi et al. 2019). The proper motion can also be used to estimate the time that V4641 Sgr has spent at its current position. Adopting a distance of 6.2 kpc places V4641 Sgr more than 500 pc below the Galactic plane (400 and 670 pc for 5 and 8 kpc, respectively). X-ray binary systems located far from the

Galactic Plane are usually explained as a consequence of natal kicks from their progenitor supernova event (e.g. Blaauw 1961). Salvesen & Pokawanvit (2020) traced the orbital trajectory of V4641 Sgr backwards in time through the Milky Way galaxy for 1 Gyr, using its current position and velocity as initial conditions. The authors constrain the most recent Galactic-plane crossing to have happened approximately 10 Myr ago. This implies that V4641 Sgr has moved at least $\approx 5^\circ$ in Galactic latitude in that time, implying that ≈ 2 Myr ago, V4641 Sgr was likely located $\approx 1^\circ$ away from its current location. Consequently, even if the system were older than a few million years, any earlier evidence of particle acceleration would not be found at its current location.

The detection by HAWC prompted a renewed interest in V4641 Sgr at different wavelengths. X-Ray Imaging and Spectroscopy Mission (XRISM) observations of the source, following an X-ray flare in September 2024, revealed the presence of an additional extended X-ray emission around the binary (Suzuki et al. 2025). The reported X-ray emission has a much smaller spatial extent than the extended HAWC detection, with a Gaussian radius of 7 ± 3 arcmin (the field-of-view of the Xtend instrument aboard XRISM is 38×38 arcmin), but large enough to be independent of the flaring episode since the corresponding physical extent is $(13 \pm 5)d_{6.2\text{kpc}}$ pc. The nature of the emission (thermal/non-thermal) could not be determined. If it is of thermal origin, it would require jet luminosities comparable to L_{Edd}. If instead, the observed emission is synchrotron radiation from a completely unrelated population of accelerated electrons, it would require $B \gtrsim 8 \mu G$ so as to not over-produce gamma rays via inverse Compton scattering in the XRISM emission region compared to the spectra measured by HAWC (Suzuki et al. 2025).

3. Observations and data analysis

3.1. The H.E.S.S. telescopes

H.E.S.S. is an array of IACTs located in Namibia, sensitive to gamma rays ranging from tens of GeV to tens of TeV. The array consists of five Cherenkov telescopes: four with mirror diameters of 12 m (referred to as CT1-CT4) placed in a square configuration and a single telescope at the centre (CT5) with a mirror diameter of 28 m. The 12-m telescope array is sensitive to gamma rays of energies above ≈100 GeV (H.E.S.S. Collaboration et al. 2006) and has a fieldof-view (FoV) of 5° diameter, while the central, large telescope is able to detect fainter Cherenkov light, which in turn translates to lower gamma-ray energies (Holler et al. 2015; Unbehaun et al. 2025). H.E.S.S. started operations in 2003, when it comprised only CT1-4. This period of operation is referred to as the H.E.S.S. I phase. The cameras of these telescopes were upgraded in 2016 (Ashton et al. 2020), starting the phase referred to as H.E.S.S. IU. The central telescope, CT5, was built in 2012, and the full array configuration is referred to as H.E.S.S. II. The CT5 camera was upgraded in 2019 (Bi et al. 2022).

3.2. Data selection and event reconstruction

H.E.S.S. observations are conducted in runs of typical duration 28 min. The region around V4641 Sgr was observed for a total of only 16 runs in the H.E.S.S. I era (H.E.S.S. Collaboration et al. 2018a). The bulk of the data was taken following the report by

the HAWC observatory in 2022¹ using the H.E.S.S. IU cameras. The system was observed in 2022, 2023 and 2024, resulting in a total of 268 runs, corresponding to almost 125 h of observations. Criteria to select good-quality runs include atmospheric transparency (ranging between 0.7 and 1.3, where 1 is the nominal value) and night-sky-background noise (NSB). When runs were taken with normal trigger settings, an NSB threshold of 700 MHz (measured by CT5) was applied to remove runs taken under bright moonlight conditions. This NSB noise cut is not required for runs taken with specific moonlight trigger settings. After these quality cuts, a total of 211 runs remained, 84 of which taken using specific moonlight trigger settings, which translates to a total observing time slightly above 100 h. Correcting for the fact that the acceptance is not uniform across the FoV and instead decreases with increasing offset from the pointing position, the equivalent on-axis exposure is 97 h. Because the majority of the data is the result of dedicated observations with pointing positions distributed around V4641 Sgr with offsets of 0.7°, the exposure across the region of interest is uniform, with less than 1% variation within a radius of 0.7°.

H.E.S.S. records stereoscopic images of atmospheric showers created by high-energy particles or gamma rays as they impact the Earth's atmosphere. After an initial reconstruction of shower geometry (Hillas 1985) the shower images were selected for gamma-likeness using a Boosted Decision Tree classifier as described in Ohm et al. (2009). The classifier cuts are optimised for a faint source with a $\frac{dN}{dE} \propto E^{-2}$ spectral shape, usually referred to as hard cuts. These cuts include a 200 photoelectron requirement for the total charge deposited by the shower in at least one of the images recorded. This requirement increases the energy threshold, but also improves the signal-tonoise ratio, especially at several TeV. Final event parameters were determined by reconstructing the selected events using the ImPACT (Parsons & Hinton 2014) algorithm, which uses a maximum-likelihood framework to fit a library of simulated templates to the recorded images. This process resulted in an estimate for the gamma-ray energy and direction, among other parameters. Using ImPACT for the event reconstruction translates to significant improvements in the angular resolution, which for this analysis resulted in a 68% containment of the point-spread function (PSF) which ranges between 0.05° (below 10 TeV) and 0.06° (above 10 TeV). In the data analysis presented in this paper, only information from CT1-4 was used for these steps.

The instrument response functions (IRFs) were derived from Monte Carlo simulations of air showers which were then reconstructed in the same way as the data. A background model, which describes the properties of the hadronic background that is incorrectly classified as gamma-like, was derived using observation runs with mostly extragalactic pointing positions in which expected gamma-ray sources are masked. The background model varies between runs due to different pointing altitude positions and hardware epochs (Mohrmann et al. 2019).

3.3. Data reduction and analysis

We used *Gammapy*-1.2 (Donath et al. 2023; Acero et al. 2024) to reduce and analyse the data. The selected gamma-like events were binned into a three-dimensional square sky-map of 6° width and 0.01° bin size, centred at the position of V4641 Sgr. The third dimension corresponds to the energy axis, which comprises 16 bins equally spaced in logarithmic energy between 0.4

and 80 TeV. For each run, a safe energy range was derived, defined as the range in which the energy is well-reconstructed, i.e. the energy bias is less than 10% (H.E.S.S. Collaboration et al. 2006), resulting in an energy range of 0.8 to 22 TeV across the dataset.

For each individual run, the counts predicted by the background model outside of a source exclusion mask were fit to those measured in the same region using two parameters that modify the overall background normalisation and spectral shape, respectively. This procedure corrects the background model for possible variations due to atmospheric conditions and instrumental characteristics, as described in Mohrmann et al. (2019). The exclusion mask defined to cover known and expected gamma-ray sources in the V4641 Sgr field of view is composed of a circle centred on the position of V4641 Sgr with radius 0.8° , a circle of 0.2° radius around the position of M28, a nearby (1.3° from V4641 Sgr) globular cluster known to host several millisecond pulsars, and a circle of radius 0.5° around the closest (2.8° from V4641 Sgr) known GeV pulsar, PSR J1809-2332 (Abdo et al. 2010).

The IRFs were projected onto multi-dimensional sky-maps. The set of maps corresponding to each observation was stacked by adding the counts and background maps and combining the IRFs weighted by the exposure of each run, considering only the energy range determined as safe for each observation. The analysis results were confirmed by an independent analysis chain. This cross-check analysis employs an independent calibration, reconstruction and background suppression (de Naurois & Rolland 2009).

Significance maps were generated using a maximum-likelihood ratio test which compared the number of measured counts to the expected counts from the combination of a source and the background. In particular, we produced significance maps assumptions: a Gaussian kernel of 2, and two different spatial assumptions: a Gaussian kernel of full-width at half maximum 0.06° (similar to the 68% containment of the H.E.S.S. PSF) and another one of 0.12° to facilitate visual comparisons with the HAWC significance maps. The final significance map reflects smoothing by the combination of these kernels with the H.E.S.S. PSF.

To describe the properties of the emission, we fitted combined spatial and spectral models within a maximum-likelihood framework using *Gammapy*. For each model, we derived the test-statistic (TS) as the Poisson log-likelihood of the data. The difference in TS between two nested models follows a χ^2 distribution with N_{dof} degrees of freedom, where N_{dof} is the difference in number of parameters between the nested models. We used this relation to convert ΔTS to significances (σ).

For each model component, we derived flux points by splitting the entire energy range into smaller bins and fitting a normalisation factor to the prediction of the model in each bin, keeping the spectral shape fixed to that of the global fit. If the significance of the model in that energy bin is less than 2σ , the 95% confidence upper limit was derived and shown instead.

In addition to flux maps, we derived flux profiles along a given spatial direction by defining rectangular regions orthogonal to that direction. Inside of each region, the measured counts were compared to the background and fitted to a spectral model with fixed spectral index. We compared this approach to using rectangular spatial templates in a spectro-morphological model, which would take into account contamination between regions due to the finite PSF. This approach yielded consistent results. We therefore kept the simple approach to avoid the need for spatial assumptions within the rectangular regions.

¹J. Goodman, Contribution to the 7th Heidelberg International Symposium on High-Energy Gamma-Ray Astronomy

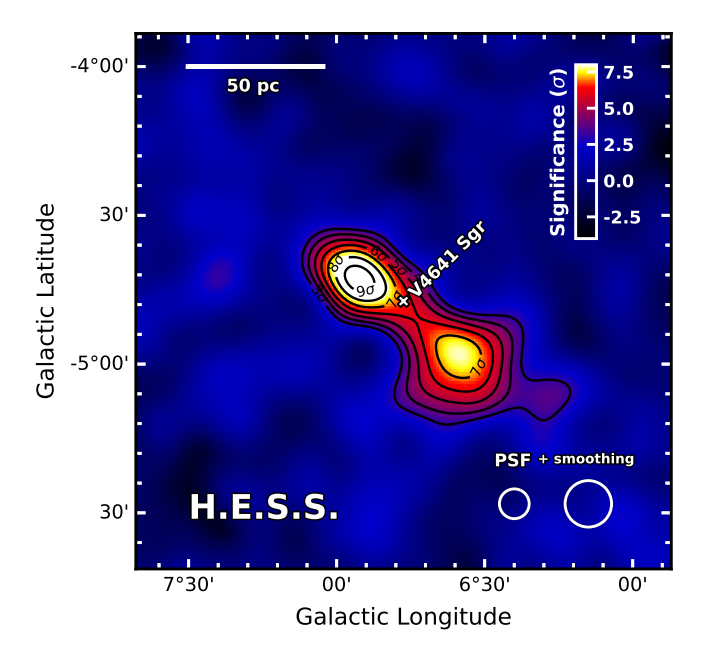


Fig. 1. Statistical significance of the H.E.S.S. excess counts with energies higher than 0.8 TeV above the background of nearly isotropic cosmic rays (indicated by the colour scale) before statistical trials were accounted for. The 68% containment region of the H.E.S.S. PSF is denoted with a white circle (left). The map was derived using a maximum likelihood test for a Gaussian kernel of radius 0.06°, which resulted in smoothing. The scale resulting from the combination of the PSF and this kernel is shown with another white circle (right).

Systematic uncertainties in the model parameters were calculated with a Monte Carlo-based approach following H.E.S.S. Collaboration et al. (2023). Details are provided in Appendix A.3.

4. Results

Figure 1 shows the significance map of the region around V4641 Sgr in Galactic coordinates. An elongated excess is detected, and the peak significance is 9.6σ . As a check of the background model, we constructed the background significance distribution by excluding the signal region with a circular mask with a radius of 0.7° centred on V4641 Sgr (Figure A.1). Fitting a Gaussian function to this distribution yielded a mean of (-0.020 ± 0.007) and a width of (1.006 ± 0.007) . The deviation of the mean and width from 0 and 1 respectively translate to a marginal shift in the significance values: the corrected peak significance is 9.5σ .

4.1. Morphology and spectrum of the emission

The first and simplest model we considered (model A) is the combination of an elliptical Gaussian spatial model² with a power-law spectrum $\left(\frac{dN_{\gamma}}{dE} = \phi_0 \times \left(\frac{E}{E_0}\right)^{-\Gamma}\right)$. The choice to start with an extended elliptical morphology was motivated by the overall shape of the emission in the significance map. We fixed the reference energy E_0 to 2 TeV for this and all other models considered. This leaves seven free parameters: the spectral normalisation and index (ϕ_0, Γ) , the centre of the elliptical

Gaussian (l, b), the semi-major axis size (σ_{major}) , the ellipticity (e), defined as $e = \sqrt{1 - \frac{\sigma_{\text{minor}}^2}{\sigma_{\text{major}}^2}}$, and the rotation angle of the major axis measured counter-clockwise from Galactic north (θ) . Including this source model in addition to the background model translates to a change in the test-statistic $\Delta TS = 193.45$ which, when accounting for $N_{dof} = 7$, corresponds to a significance of 12.9σ . The best-fit parameters of this model are summarised in Table 1. The resulting spectrum and 68% containment region of the Gaussian are shown in Figure 2. The measured spectral index of $\Gamma = 1.82 \pm 0.27_{stat} \pm 0.07_{syst}$ is among the hardest measured for Galactic sources in this energy range (H.E.S.S. Collaboration et al. 2018b). We found no evidence for curvature in the spectrum ($\Delta TS=1.07$) or an exponential cut-off ($\Delta TS=1.01$). The peak significance in the residual significance map produced after subtracting the model is 3.1σ . The distribution of residual significance values are fitted by a Gaussian function of mean of (-0.022 ± 0.003) and a width of (0.986 ± 0.003) , consistent with a well described signal and a well normalised background.

The single elliptical component has a major axis of $\sigma_{\rm major} = 0.34 \pm 0.04^{\circ}_{\rm stat}^{3}$. The model is significantly (5σ) extended also in the minor axis direction: the best-fit ellipticity corresponds to $\sigma_{\rm minor} = 0.06 \pm 0.01^{\circ}_{\rm stat}$. Accounting for distance, the 68% containment radii of the spatial model $(1.5\sigma_{\rm major/minor})$ for a 2D Gaussian) correspond to $\sigma_{\rm major} = (55.4 \pm 6.3_{\rm stat})d_{\rm 6.2kpc}$ pc and $\sigma_{\rm minor} = (9.8 \pm 2.0_{\rm stat})d_{\rm 6.2kpc}$ pc. We found that the position of the microquasar does not correspond with the best-fit centroid of the model: the angular distance between them is $0.124 \pm 0.032^{\circ}_{\rm stat}$, which corresponds to a physical distance of more than $10d_{\rm 6.2kpc}$ pc and which is inconsistent with zero by almost 4σ . In particular, the model centroid lies south (along the axis of the emission) of the position of the binary.

To test the assumption of a Gaussian morphology, we repeated the fit with an additional parameter η which parametrises the shape between a flat elliptical disk morphology ($\eta=0.01$) and a peaked elliptical Laplace profile ($\eta=1$)⁴. A Gaussian shape is recovered when $\eta=0.5$. Freeing η only marginally improved the fit, with $\eta=0.25\pm0.13_{\rm stat}$ preferred by 1.5σ . All other parameters fitted remained consistent within 1σ uncertainties (see Table A.1). We concluded that the morphology is consistent with a shape in between an elliptical flat disk and an elliptical Gaussian, but we cannot distinguish between this scenario and the usually assumed Gaussian shape.

4.1.1. Broad-band spectral energy distribution

The H.E.S.S. spectral measurement and the existing measurements by *Fermi*-LAT (Zhao et al. 2025), HAWC (Alfaro et al. 2024) and LHAASO (LHAASO Collaboration 2024b) reveal the full shape of the gamma-ray component in the spectral energy distribution. The H.E.S.S., HAWC and LHAASO spectral measurements connect smoothly, as can be seen in Figure 3. The H.E.S.S. data and the *Fermi*-LAT upper limits imply a rising spectral energy distribution in the 1-20 TeV range. HAWC and LHAASO data then show the turnover at energies around 100 TeV. All together, the data reveal, for the first time, a source spectrum which peaks at energies greater than 100 TeV.

²https://docs.gammapy.org/1.2/api/gammapy.modeling. models.GaussianSpatialModel.html

³In the following discussion of morphology parameters, we quote only statistical errors, see Table 1 for systematics errors

⁴https://docs.gammapy.org/1.2/api/gammapy.modeling. models.GeneralizedGaussianSpatialModel.html

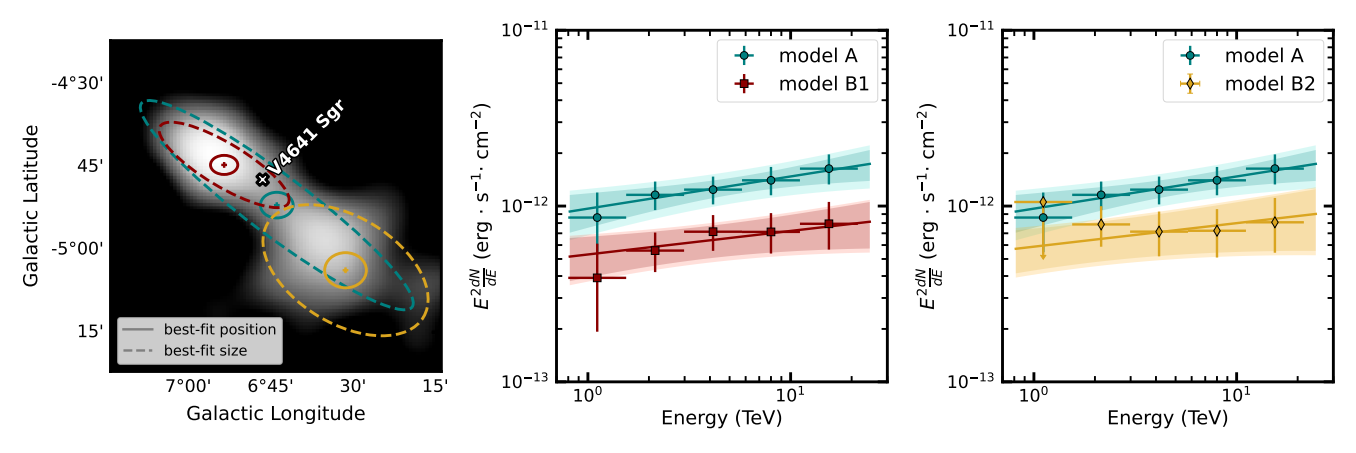


Fig. 2. Left: Significance map. The 68% containment regions (corresponding to 1.5σ for a 2D Gaussian) of the spatial models are overlaid. The best-fit extent is depicted with dashed lines in teal for model A (see Section 4.1), and in red and yellow for models B1 and B2 (see Section 4.1.2), respectively. The best-fit position and its 95% confidence intervals are shown with crosses and solid lines using the same colour scheme. Middle: The measured spectral energy distribution (SED) for models A (teal circles) and B1 (red squares). The solid line depicts the spectral shape of the best-fit power law. The dark and light shaded areas depict the statistical and systematic error bands, respectively. The error bars represent the combined systematic and statistical errors. The upper limits are shown at the 95% confidence level. Right: The symbols follow those of the middle panel, but for models A and B2 (yellow diamonds).

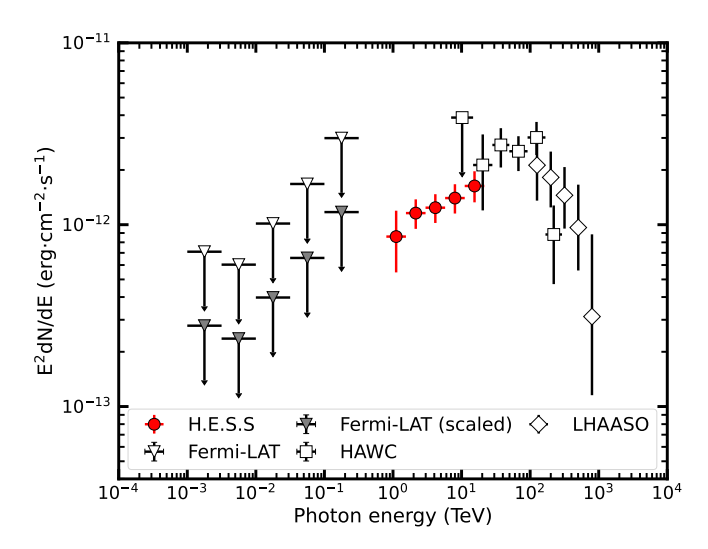


Fig. 3. Broad-band spectral energy distribution. Flux points and upper limits measured by H.E.S.S. (red circles), HAWC (squares), LHAASO (diamonds), and *Fermi*-LAT. The *Fermi*-LAT points are shown both as published in Zhao et al. (2025) (light triangles) and re-scaled to the H.E.S.S. emission region size (dark triangles). The broad-band spectrum is observed to rise sharply until a peak forms at energies of ≈ 100 TeV, further extending up to energies of several hundreds of TeV.

In the GeV band we adopt the flux upper limits from Zhao et al. (2025), both as published and also rescaled

down by a factor 2.6 to account for the fact that the extraction region in Zhao et al. (2025) is not de-convolved with the LHAASO angular resolution, almost an order of magnitude larger than that of H.E.S.S. The factor 2.6 is conservatively derived as the ratio between the angular size of the region with significance $> 5\sigma$ in the LHAASO significance map and the 95% containment region of model A (1326 arcmin²).

4.1.2. One or two components?

The significance map shown in Figure 1 suggests the presence of two peaks in the morphology of the emission, as also indicated by Alfaro et al. (2024). We tested this hypothesis by adding a new component to the model, a second elliptical Gaussian spatial model with a power-law spectrum. We found weak statistical preference (3σ) for the inclusion of a second component. Among the different scenarios considered (see Tables 1 and A.1), the best statistical description when accounting for N_{dof} is two components with identical spectral index and orientation angle (model B, with components B1 and B2). Allowing more or all parameters to vary independently (models C and D, see Appendix A.2) did not improve the fit and resulted in statistically consistent best-fit parameters, in part because of increasing uncertainties. In particular, the ellipticity and inclination angle of the second component are poorly constrained when allowed to vary independently. We will consider the B model as the reference twocomponent scenario, but will take into account the spread of the

 Table 1. Best-fit parameters for the different spectro-morphological models.

Model	ϕ_0	Γ	E_0	l	b	$\sigma_{ m major}$	$\sigma_{ m minor}$	e	θ
	ϕ_0 (10 ⁻¹³ TeV ⁻¹ cm ⁻² s ⁻¹)		(TeV)	(deg)	(deg)	(deg)	(deg)		(deg)
		sir	gle ellipt	ical component,	$TS_A = 92320.849$				
A	$1.71^{\pm 0.27_{stat}}_{\pm 0.07_{syst}}$	$1.82^{\pm 0.11_{stat}}_{\pm 0.05_{syst}}$	2	$6.731^{\pm 0.033_{stat}}_{\pm 0.005_{syst}}$	$-4.866^{\pm0.026_{stat}}_{\pm0.005_{syst}}$	$0.34^{\pm 0.04_{stat}}_{\pm 0.01_{syst}}$	$0.06^{\pm 0.01_{stat}}_{\pm 0.01_{syst}}$	$0.984^{\pm 0.005_{stat}}_{\pm 0.001_{syst}}$	53.0 ± 2.2
	two c	components, s	hared ang	gle and index, (\Delta	$\Delta TS_A = 19.8, \Delta N_d$	$t_{of} = 5 \rightarrow 3.2a$	r)		
B1	$0.91^{\pm 0.20_{stat}}_{\pm 0.10_{syst}}$	$1.87^{\pm0.11_{stat}}_{\pm0.03_{syst}}$	2	$6.891^{\pm 0.027_{stat}}_{\pm 0.003_{syst}}$	$-4.745^{\pm 0.019_{stat}}_{\pm 0.003_{syst}}$	$0.15^{\pm 0.05_{stat}}_{\pm 0.01_{syst}}$	0.04 ± 0.02	0.958 ± 0.037	$58.9^{\pm 4.6_{stat}}_{\pm 7.8_{syst}}$
B2	$1.01^{\pm 0.26_{stat}}_{\pm 0.08_{syst}}$	-	2	$6.523^{\pm0.042_{stat}}_{\pm0.005_{syst}}$	$-5.063^{\pm0.035_{stat}}_{\pm0.005_{syst}}$	$0.18^{\pm 0.05_{stat}}_{\pm 0.04_{syst}}$	0.11 ± 0.05	0.810 ± 0.15	-

parameters in models C and D when discussing physical implications. The best-fit parameters of models C and D are collected in Table A.1.

When considering two components, their 68% containment radii in the major axes are $(24.5 \pm 8.2_{\rm stat})d_{6.2\rm kpc}$ and $(29.7 \pm 7.5_{\rm stat})d_{6.2\rm kpc}$ pc for the first and second component, respectively. Corresponding values for the minor axes are $(7.0 \pm 3.8_{\rm stat})d_{6.2\rm kpc}$ and $(17.5 \pm 7.6_{\rm stat})d_{6.2\rm kpc}$ pc. The extension along the minor axis is only weakly constrained in this scenario, with best-fit values of $\sigma_{\rm minor}$ consistent with zero within $\approx 2\sigma$. In any case, a scenario with two point sources, as considered in Alfaro et al. (2024), can be clearly excluded.

The relative sizes of the two components are marginally dependent on whether the orientation angle is allowed to differ between them, but are always consistent with each other within statistical uncertainties. We found that V4641 Sgr does not lie halfway between both components, as one would naively expect in a symmetrical jet lobe scenario like that observed in SS 433. Instead, it is much closer to the centroid of the B1 component than B2 $(0.125 \pm 0.019^{\circ}_{stat})$ vs $0.371 \pm 0.035^{\circ}_{stat}$, falling within the 68% containment region of B1. This finding is consistent with the offset between the centroid of model A and the position of V4641 Sgr discussed in the previous section. Similar distances were found for any of the other two component models considered (see Table A.1). The corresponding projected physical

distances between V4641 Sgr and the centroids in the models considered are in the range (10-15) $d_{6.2\mathrm{kpc}}$ and (35-40) $d_{6.2\mathrm{kpc}}$ pc for the first and second components, respectively. The centroids of the two components are separated by $0.486 \pm 0.040^{\circ}_{\mathrm{stat}}$, which corresponds to over $50d_{6.2\mathrm{kpc}}$ pc.

In any scenario with two components, the overlap between them is non-negligible, leading to significant emission across the entire region, with no discernible gap between them. In particular, by fitting a modified version of model A with a gap centred on V4641 Sgr of total height h, we were able to place an upper limit on how large this gap can be. We found that $h < 0.06^{\circ}$ (95% containment), which translates to $6.5d_{6.2\text{kpc}}$ pc. The same exercise around the centroid of model A yielded $h < 0.15^{\circ}$ (95% containment), consistent with the weak preference for the two-component model.

4.1.3. Spatial profiles

To study the morphology in a model-independent way, we extracted the flux inside regions defined across and along the emission. The peculiar shape of the gamma-ray emission and the fact that V4641 Sgr is not located at its centre require a clear definition of the along and across directions. The resulting profiles are one-dimensional and calculated as a function of distance to V4641 Sgr. We defined both the across and along directions such

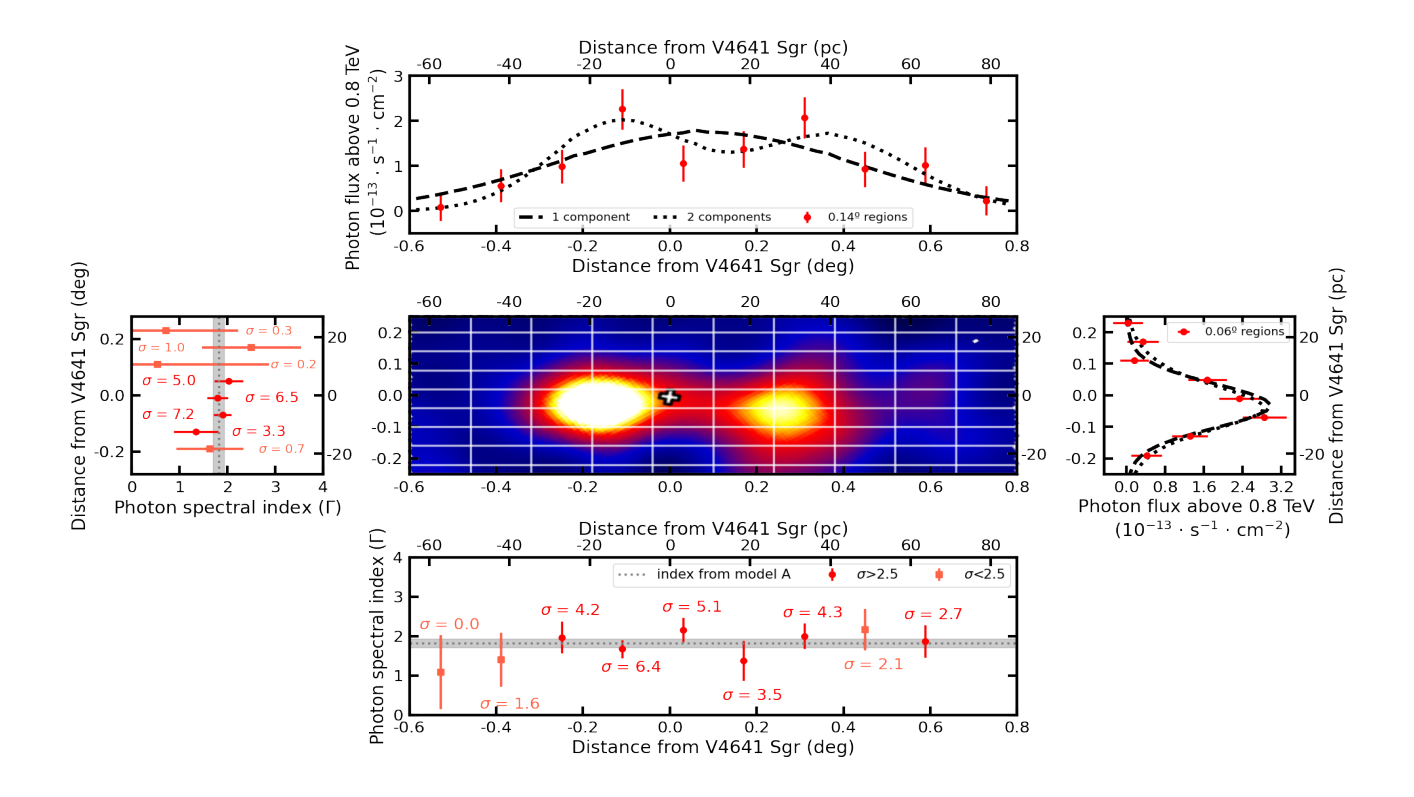


Fig. 4. Profiles along and across the emission. *Centre:* Rotated and scaled version of the significance map is shown to help visualise the geometry of the different regions used to derive profiles. *Top:* The red circles represent the measured flux above 0.8 TeV along the major axis as a function of distance to V4641 Sgr. Distances are provided in degrees and parsecs adopting a distance of 6.2 kpc. The dashed and dotted lines depict the predictions of models A and B, respectively. *Bottom:* The gamma-ray spectral index measured along the major axis in the same regions. Square and round symbols indicate when emission is detected inside the region with significance below or above 2.5σ , respectively. A dotted grey line and shaded region indicate the best-fit value and statistical uncertainty of the index parameter in model A. The best-fit index at distance $\approx 0.7^{\circ}$ is negative and is thus not visible in the plot. The significance of the emission in that region is 0.3σ . *Middle left:* The symbols follow those of the bottom panel, but measured across the emission region. *Middle right:* The symbols follow those of the top panel, but measured across the emission region.

that they pass through the microquasar position. We also derived profiles using the best-fit position of model A as a reference position and found the overall shape of the profiles to be highly consistent. We defined the direction we refer to as along the emission by fitting a combined spectral and spatial model like model A, but with the position fixed to that of V4641 Sgr. This yielded $\theta = 55.06 \pm 3.33^\circ$, which is consistent with the best-fit θ of model A (see Table 1). The model with fixed position has $\Delta TS_A = -24.49$, which accounting for the extra two degrees of freedom rejects the model where the position is fixed to that of V4641 Sgr by 4.6σ . The across direction is taken orthogonal to the along direction.

The fact that V4641 Sgr is at the origin of the chosen coordinate system slightly obscures that in 2D, the position of V4641 Sgr is not consistent with the centroid of model A or with the dip between models B1 and B2 as discussed above, due to projection effects. The central panel of Figure 4 shows a rotated version of the significance map to aid the reader in visualising the geometry of the regions discussed. To measure the flux in each of the regions we fixed the spectral index to $\Gamma=1.8,$ consistent with the index of the overall region. Further, we repeated the exercise with free Γ to measure the spectral index in the different regions.

Flux and spectral index profiles along the emission To measure the flux profile we used 10 rectangular regions of height 0.5° ($\approx 5 \times \sigma_{minor}$ of model A) orthogonal to the line defined by Galactic coordinates (7.2658°,-4.4455°) and (6.1181°,-5.2472°). Dividing this line into 10 sections translates to a region width

of 0.14°, equivalent to more than the 95% containment radius of the H.E.S.S. PSF. The flux profile can be seen in the top panel of Figure 4. The shapes derived from Models A and B are also shown. The resulting flux was scaled to the solid angle size of the 10 regions used for the measurements. We did this for both model A and B and produced flux predictions. As can be seen, the flux profiles confirm the weak preference for a model with two components.

To measure the spectral index we used slightly different regions, of same width, but reduced height of 0.25° (95% containment of the minor axis of model A) in order to improve the signal-to-noise ratio. The procedure is the same as before, but with an additional free parameter (the index) in the fit. The best-fit index values can be seen in the bottom panel of Figure 4. We identified relevant regions with a significance threshold of 2.5σ , and found that in all cases, the spectral index is consistent with that of the full region. No trend or pattern in the index can be discerned.

Flux and spectral index profiles across the emission We repeated the same procedure, but now with boxes of 0.06° height and 1.2° width. The flux and index profiles can be found in the left and right panels in Figure 4, respectively. The profile confirms that the emission is significantly extended in this direction (the H.E.S.S. angular resolution is $\approx 0.05^{\circ}$), and again no trend or pattern can be discerned in the spectral index distribution, which is consistent with the average value.

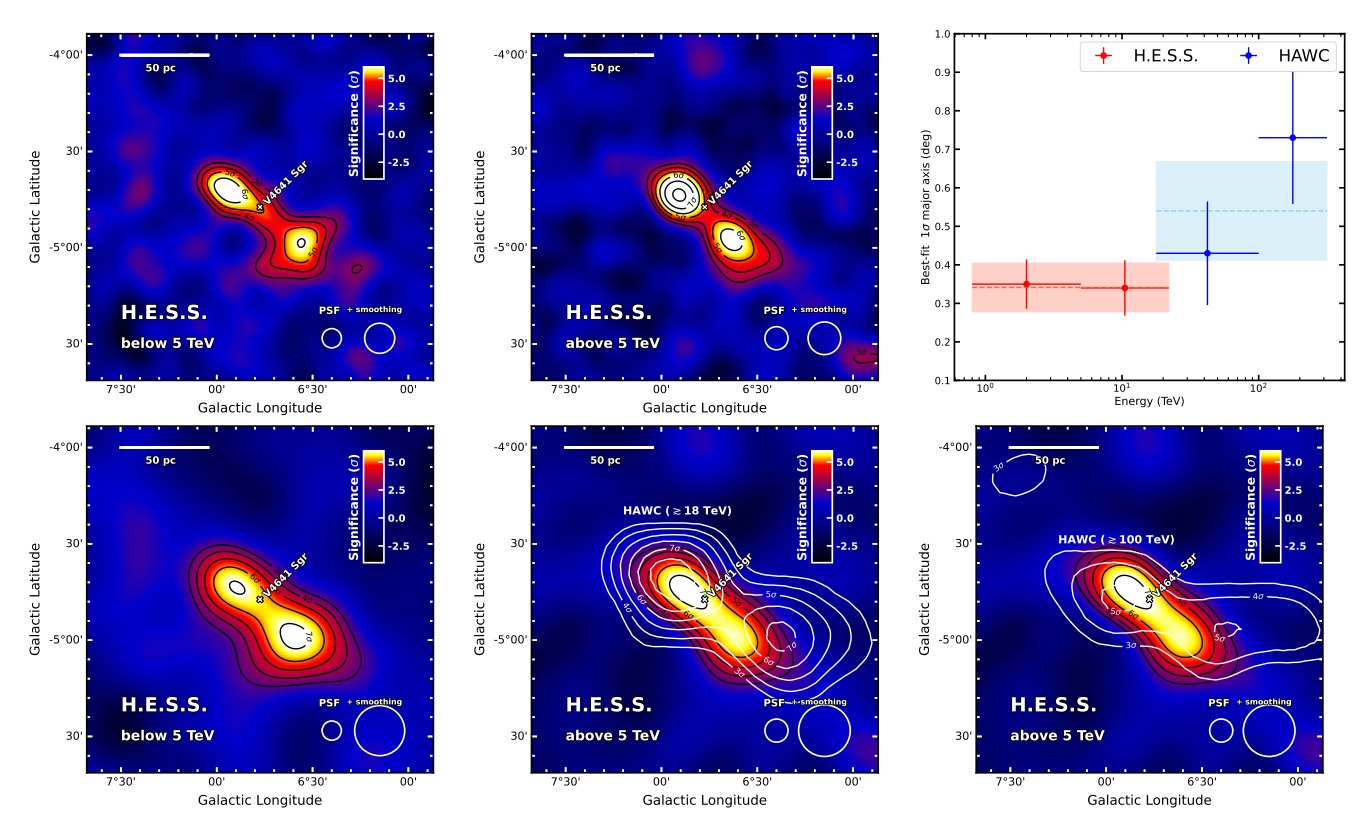


Fig. 5. Significance maps in the energy bands. The symbols and colours follow those of Figure 1, but for photon energies below 5 TeV (top left) and above (top middle). Significance maps derived with a larger smoothing kernel of 0.12° are shown in the bottom row. The map for photon energies above 5 TeV is repeated to show the contours from the two HAWC significance maps provided in Alfaro et al. (2024). Finally, the top right panel shows the size of the major axis in the "model A" fit for both H.E.S.S. (red points) and for the HAWC publicly available data (blue points). The dashed lines and shaded bands represent the best-fit size and uncertainty derived in larger energy ranges as presented in Table 1 and Alfaro et al. (2024). The error bars/bands represent the combined statistic and systematic uncertainty.

4.2. Energy-dependent morphology

We explored the possibility of an energy dependent morphology in two ways: we split the data into two energy ranges: from 0.8 to 5 TeV and from 5 to 22 TeV (low and high energy, respectively) and we repeated the profile estimation described above and the fits described in Section 4.1. We found no evidence of energy-dependent morphology in either of these tests. Figure 5 shows the significance maps derived in each of the energy ranges.

In particular, we considered energy-dependent morphology in both the single and two-component model scenario. When fitting one elliptical component (with fixed spectral index) in the two energy bands, every parameter was consistent well within statistical uncertainties, both between energy ranges and with the fit across all energies. When considering the two-component model we also froze the angle θ and photon spectral index to those of model B. We found a weak hint that the first component becomes more symmetrical at higher energies, which can also be seen in Figure 5. The fit results have large statistical errors, however, with $e_{B1}^{>5 \text{ TeV}} = 0.01 \pm 0.51$ when both components were fitted together (which translates into an upper limit of $e_{B1}^{>5}$ TeV < 0.82, 95% C.L.) and $e_{B1}^{>5}$ TeV = 0.67 ± 0.36 when the second component was frozen. All other parameters such as position or morphology at low energies remained consistent with those of model B. We conclude that there is no significant evidence for energy-dependent morphology in either the one or two component scenario.

While we do not find evidence of energy-dependent morphology within the H.E.S.S. energy range, there might be when comparing our measurements to others made at a higher energies. In particular, the best-fit value of the major axis of model A $(\sigma_{major}=0.34\pm0.04\pm0.01^\circ)$ is smaller than the one measured by HAWC $(\sigma_{major}=0.54\pm0.08\pm0.1^\circ,$ Alfaro et al. 2024), although consistent within 1.5σ statistical and systematic uncertainties. Figure 5 shows H.E.S.S. significance maps above and below 5 TeV using both the usual kernel of 0.06° and a larger kernel of 0.12° which results in a total smoothing on the order of the angular resolution of HAWC, to facilitate visual comparisons between the instruments. Comparing these maps with the HAWC contours visually suggests a trend with energy.

To explore this possibility further, we made use of the publicly available dataset and analysis scripts provided by the HAWC Collaboration⁵ to repeat the fit with a single elliptical component reported by Alfaro et al. (2024), but restricting the energy ranges to above and below 100 TeV. The best-fit $\sigma_{
m major}$ for both the H.E.S.S. and HAWC energy-restricted fits is shown in Figure 5. As can be seen, the extension measured with the HAWC data below 100 TeV ($\sigma_{\rm major} = 0.43 \pm 0.09 \pm 0.1^{\circ}$) is in better agreement with the size measured by H.E.S.S. at lower energies. Above 100 TeV, however, the size almost doubles to $\sigma_{\rm major} = 0.74 \pm 0.14 \pm 0.1^{\circ}$. This is likely caused by the 3-4 σ "tail" towards lower longitudes which can be seen in the HAWC contours above 100 TeV in Figure 5. Here we have assumed that the HAWC systematic uncertainty does not depend on energy. Nevertheless, even when comparing this measurement with that of H.E.S.S. in the lowest energy range, the difference between them is less than 2.5σ . We conclude that there is no significant evidence of energy-dependent morphology, neither in the H.E.S.S. data alone nor when comparing with HAWC results.

4.3. Time variability

We searched for time variability in the region surrounding V4641 Sgr with a focus on small spatial scales. The H.E.S.S. observations probe timescales ranging between several minutes and several years - shorter than the light-travel time of a few parsecs. Consequently, we would only expect variability to occur on smaller regions and not the entire gamma-ray emission. We considered four regions of 0.07° radius (>68% containment for a point source, $\approx 7d_{6.2\text{kpc}}$ pc): one centred on V4641 Sgr, and three on the best-fit positions of models A and B. We derived light-curves in run-wise, monthly and yearly timescales. No variability is found in any of the regions, nor from a larger region that contains the entire gamma-ray emission.

4.4. Contributions from the central source

Significant gamma-ray emission is detected from the position of V4641 Sgr. When the extended components are not included in the fit, a point-like source model fixed to the microquasar coordinates provides a 4σ improvement in the test-statistic; comparing the measured counts in a region of radius 0.1° around V4641 Sgr to the background reveals a significant (4.8 σ) excess. When the contribution from the extended model components detailed in Table 1 is accounted for, however, the equivalent significance values drop to below 1σ . We derived upper limits for a possible additional contribution from the central source by including an additional point-source component fixed to the position of V4641 Sgr in the model. The spectrum is assumed to be a power-law with a spectral index of 2. The fit is repeated, allowing the relevant parameters of the extended model(s) and the point-like source to vary. The result of this calculation is obviously impacted by the choice of model to describe the extended emission surrounding V4641 Sgr. We derived upper limits using models A, B and D and find differences of at most 20% between the resulting flux upper limits. Machine-readable upper limits (including likelihood profiles) are provided in the online material (H.E.S.S. Collaboration 2025) for model B, but for simplicity, and irrespective of the model, the 95% differential flux upper limits $(E^2 dN/dE)$ between 0.8 and 22 TeV are contained within the range $(0.45 - 1.3) \times 10^{-13}$ erg cm⁻² s⁻¹.

5. Estimating the gas density around V4641 Sgr

A critical piece of information for the interpretation of the gamma-ray emission is the presence of dense gas in the surroundings which could act as a target for proton interactions. We used a combination of publicly available data products and dedicated observations with the Nobeyama Radio Observatory (NRO) to characterise the gas around V4641 Sgr.

Dedicated ¹²CO(J=1-0) measurements were obtained with the NRO 45 m radio telescope between February and March 2025. An area of 0.8 × 1.4° centred at R.A.=274.87°, Dec = 25.66° was scanned in constant declination bands. The total observation time added up to roughly 20 h. The beamwidth of the NRO 45-m telescope is 15", a significant improvement compared to other existing CO observations of the region, such as the Dame 2022 survey (Dame & Thaddeus 2022), with a beamwidth of 500". A few small clouds were identified, none at a distance consistent with V4641 Sgr nor resembling the gamma-ray morphology. Figure 6 shows the velocity spectrum averaged inside the gamma-ray emission region, and an RGB map indicating the new clouds which were discovered. No molecular gas was found at a distance consistent with any estimates of the distance

⁵https://data.hawc-observatory.org/datasets/V4641/index.php

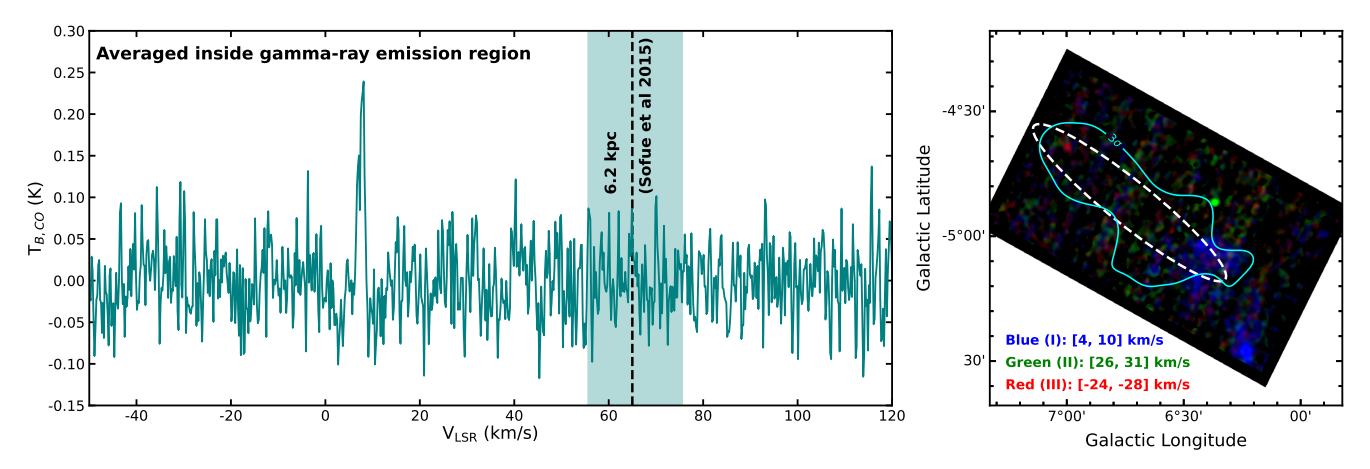


Fig. 6. Molecular gas around V4641 Sgr. *Left*: The brightness temperature profile of the CO emission averaged inside of the 68% containment region of model A. The shaded range indicates a range of 10 km s^{-1} around the velocity corresponding to the position of V4641 Sgr. Note that this shaded band is for illustration purposes only, and that the density estimate reported in the text uses the noise level across the entire velocity range measured, regardless of what distance they correspond to *Right*: The RGB image depicting the integrated CO intensity in the three velocity ranges where small clouds are identified, unrelated to V4641 Sgr. Smoothing with a Gaussian kernel of width 30 arcsec width was used to facilitate visualisation. The blue line shows the 3σ contour of the H.E.S.S. significance map (Figure 1). The dashed white line shows the 68% containment region of model A.

to V4641 Sgr, regardless of the rotation curve used for the conversion. Using the noise level in the data, we derived an upper limit of $n_{\rm gas} < 0.2~{\rm cm}^{-3}$ for the average density in the gamma-ray emitting region (defined using model A). Details on the derivation of this value and validation using archival data are described in Appendix C.

In addition to dedicated and archival CO observations, we considered the presence of atomic hydrogen through the study of 21-cm emission. We used the publicly available map from the HI4PI survey (Winkel et al. 2016) and followed the same procedure as for the CO maps, assuming optically thin gas. We found $n_{\rm HI} \approx 0.08 \ {\rm cm}^{-3}$. The HI column density map shown in Figure C.1 and the HI density estimate obtained differs significantly from those presented by Alfaro et al. (2024). In that work, an integration velocity range three times larger than the average line widths of the warm neutral medium (Kalberla & Haud 2018) was used. While the velocity range corresponds to a physical distance of almost 1 kpc (e.g. Sofue 2015), all gas is assumed to be concentrated in a 20 pc depth, resulting in a higher density estimate (≈ 1 cm⁻³) than reported here. Further details and additional checks using $H\alpha$, free-free emission, and dust maps are presented in Appendix C. Taken together, these observations reveal that V4641 Sgr is located in a low-density environment. This finding is consistent with prior expectations given the fact that the scale height of Galactic molecular gas (Heyer & Dame 2015) is several times smaller than the height of V4641 Sgr below the Galactic plane. Finally, modelling of the XRISM data under a thermal assumption yielded $n_{gas} < 0.3 \text{ cm}^{-3}$ (Suzuki et al. 2025), further supporting our conclusion.

6. Discussion

We have presented the H.E.S.S. view of the gamma-ray emission around V4641 Sgr. How this emission relates to the binary system and its jets is unclear. The reported low jet inclination angle would be expected to translate to a point-like source in analogy with the gamma-ray view of blazars, which differs significantly from the extended, asymmetrical emission we observed. In such a "microblazar" scenario in which particles are accelerated and emitting within a relativistic, low inclination jet, one would also

expect one emission component to be enhanced by beaming, the other suppressed. The consistency between the flux of models B1 and B2 requires that, in such a scenario, emission arises from either a much slower jet termination region or interaction of escaped particles with their environment (i.e. large-scale field, molecular cloud).

If the observed morphology is due to a nebula-like structure inflated by a jet (as discussed in Alfaro et al. 2024), we can relate its size to the energetics of the central engine. We define an average jet power as $\bar{L}_{\rm jet} = \int_0^{t_{\rm jet}} L_{\rm jet} dt/t_{\rm jet} = \eta_{\rm jet} L_{\rm Edd}$, where $\eta_{\rm jet}$ is the jet efficiency. Assuming the system did not move or reorientate during this period, one can follow the expressions in Begelman & Cioffi (1989) to estimate the time required to produce a jet-cocoon of full length ℓ_c as

$$t_{\rm jet} \approx \left(\frac{\ell_{\rm c}}{100 \, \rm pc}\right) \left(\frac{r_{\rm h}}{5 \, \rm pc}\right) \left(\frac{\eta_{\rm jet}}{0.1}\right)^{-\frac{1}{2}} \left(\frac{n_{\rm gas}}{0.2 \, {\rm cm}^{-3}}\right)^{\frac{1}{2}} \left(\frac{v_{\rm jet}}{0.9 c}\right)^{\frac{1}{2}} \, {\rm Myr},$$
 (1)

where r_h is the jet cocoon head radius, which we take as 5 pc motivated by the measured σ_{minor} (see Fig. 7). Note also that in Equation 1 we adopt a jet velocity $v_{\text{jet}} = 0.9c$ following Hjellming et al. (2000), but that in principle, the velocity of the jet could be much lower in some of the scenarios considered in the following discussion. We can compare this dynamical estimate with a characteristic time for mass-transfer in the binary system, taken as the thermal lifetime of the companion star $t_{\text{th}} = GM^2/2RL$, where M, R and L are its mass, radius and luminosity. Using numbers from MacDonald et al. (2014), we find $t_{\text{th}} \approx 100$ kyrs, though this number is known to provide underestimates (Langer et al. 2000; Podsiadlowski et al. 2002).

For the remaining discussion we will consider two competing scenarios with different implications for the acceleration and transport of particles in and around V4641 Sgr.

1. Jets are not aligned with the line of sight: A simple explanation for the elongated asymmetric emission is that there are jets with an orientation angle i_{jet} that is not aligned close to our line of sight. This scenario would be consistent with the reported orientation of the orbit and accretion disc (Gallo et al. 2014; Miller et al. 2002), but inconsistent

with the apparent super-luminal motion reported following the 1999 flare (Hjellming et al. 2000). The left panel of Figure 7 shows a cartoon summarising the proposed geometry. If the loss timescales of the gamma-ray emitting particles are sufficiently long, and confinement is effective, the emission could plausibly be a remnant of past activity, with the jet being currently inactive. Observationally, this means that the gamma rays would be the best tracers of these hypothetical jets, since a low-density environment could hide evidence in other wavelengths. We will refer to this scenario as the "hidden jet" scenario in the following discussion.

2. Jets are aligned with the line of sight. Another possible explanation for the observed gamma-ray morphology is that the jets are indeed aligned with the line of sight, but that particles accelerated in the jets escape into a medium with properties that produce the elongated gamma-ray morphology. A simple example would be the presence of a molecular cloud with shape similar to the gamma-ray emission, which is illuminated by the particles accelerated by V4641 Sgr. Alternatively the emission could signal the presence of a large-scale magnetic field configuration which traps the particles and leads to the observed morphology (as in, e.g. Neronov et al. 2025; Bao et al. 2025; Churazov et al. 2024). The right panel of Figure 7 shows a cartoon summarising the proposed geometry. We will refer to this scenario as the "special environment" scenario in the following discussion. Note that in this scenario, the extent and shape of the gamma-ray emission could be directly explained by the extent and shape of this special environment.

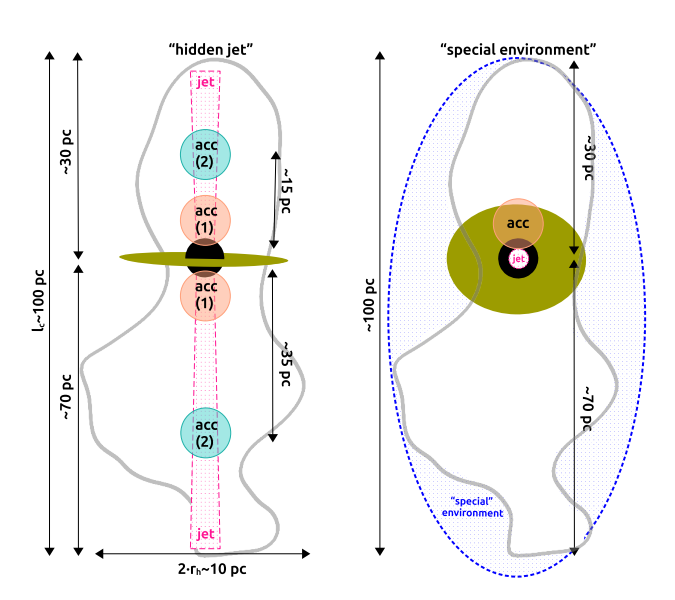


Fig. 7. Cartoon depicting the two geometries. The gamma-ray emission region is outlined with a grey line that traces the rotated 3σ contour of the map shown in Figure 1. The black hole and accretion disc are shown assuming two options for the inclination angle: almost 90° (left) or close to 0° (right). In the perpendicular case, a pair of (hypothetical) jets launching from the black hole are depicted in magenta. In the aligned jet case, a special environment that would explain the gamma-ray morphology is depicted in blue. The different acceleration sites discussed in the text are marked with circles. The sketch is annotated with scales derived from the best-fit gamma-ray models for the adopted distance of 6.2 kpc.

In the hidden jet scenario, the jets launched by V4641 Sgr have to extend around 50 pc to generate the observed morphology. In the aligned case, without resorting to a special envi-

ronment and assuming e.g. i_{jet} =10° (Hjellming et al. 2000) jets would have to extend more than 300 pc. As shown in Equation 1, producing 50 pc jets already poses tight constraints on the energetics, hence we do not elaborate further on this "very extended jet" case and require the special environment if the jet is aligned. Table D.1 summarises all the considered scenarios and their feasibility.

6.1. Possible acceleration sites

While the existing observations are insufficient to pin-point the location of an acceleration site, they provide relevant constraints. We consider the two simplest scenarios motivated by the observations, with acceleration taking place either close (≤ 3 pc) to the binary system, in the corona or near the jet base, or further out in the jets, at distances of tens of pc. When transforming the angular size of the gamma-ray emission to physical distances throughout the discussion we will always assume (unless stated otherwise) an orientation orthogonal to the line of sight. Based on the uncertainties on the geometry of the system, however, every physical distance might be greater by a factor $(\sin \phi)^{-1}$, where ϕ is the unknown real inclination. We note that $\phi = i_{\rm jet}$ in the hidden jet scenario.

- 1. Case 1: Acceleration close to the central source. If particles are accelerated somewhere near the compact object, in the corona or near the jet base (as in e.g. Markoff et al. 2005; Bosch-Ramon et al. 2005b), they would need to be transported out to ≈30 pc and ≈70 pc in each direction, respectively, while suffering minimal losses to avoid noticeable energy-dependent morphology. For simplicity, we will adopt r₁ =50×(sin φ)⁻¹ pc as the minimum distance that particles need to travel in this scenario in the following discussion. This acceleration site location is applicable in both jet geometries considered (see Figure 7), although the dominant transport mechanism would likely be advection with the hidden jet flow or diffusion within the special environment, respectively.
- 2. Case 2: Acceleration within the hidden jet. SS 433 is the only microquasar for which the particle acceleration sites have been unequivocally identified (Safi-Harb et al. 2022; Kayama et al. 2022; H.E.S.S. Collaboration et al. 2024). In that case, the particle acceleration can be localised to positions along the jets, at a few tens of parsecs distance from the central binary. In analogy with SS 433 and motivated by the weak evidence for two components in the gamma-ray emission, we consider the possibility that the acceleration sites are located somewhere in the (hypothetical) hidden jet, or its lobes/cocoon. Assuming for simplicity that these acceleration sites are consistent with the centroids of models B1 and B2, this requires particles to be transported ≈ 15 pc and ≈ 35 pc in each direction again for simplicity we will summarise this scale as $r_2 = 25 \times (\sin \phi)^{-1}$ pc.

The distinction between acceleration locations in cases 1 and 2 is most relevant in the hidden jet scenario: in the special environment scenario, particles would still have to travel a distance $\approx r_1$ to reproduce the morphology regardless of the site of acceleration within the jets (see Figure 7).

6.2. Gamma-ray emission mechanism

Translating the properties of the observed gamma-ray emission into constraints on particle acceleration and transport requires knowledge on which emission process is dominant. Electrons and positrons (hereafter referred to collectively as electrons) produce gamma-ray emission through IC scattering of soft photons to gamma-ray energies. The same electrons would also produce synchrotron emission at lower photon energies (radio to X-ray), the intensity of which is proportional to the energy density of the local magnetic field (u_B). If instead hadrons (protons and heavier nuclei) are responsible for the bulk of the emission, they would produce gamma rays via inelastic collisions with the surrounding gas.

We will consider two competing scenarios, where the entirety of the gamma-ray emission is either produced by electrons or by protons. While a combined model is possible, we will not consider such a model here. There is no evidence for two components in the gamma-ray spectra and thus it would require fine-tuning while increasing the number of free parameters.

We used the open-source GAMERA package (Hahn 2015; Hahn et al. 2022), which includes Klein-Nishina corrections for the IC scattering calculations (e.g. Blumenthal & Gould 1970), to model both the temporal evolution of the particle distributions and the resulting radiation. We compared the models to the observed broad-band spectra (Figure 3). We fitted predictions from several one-zone emission models to this data. Since the likelihood profiles of the GeV upper limits from Zhao et al. (2025) were not provided, they cannot be directly used in the likelihood fit and consistency with them was checked after fitting. For the model comparisons we included the H.E.S.S. spectra with the flux points of Model A (Figures 2 and 3) because (1) they correspond to the same spatial scale as the LHAASO measurements and (2) the spectral parameters of the two-component case are consistent, both for the analysis presented here and in the discussion in Alfaro et al. (2024). Consequently, fitting the spectra separately does not add any additional information about the parent particle population. While the two-component model is suggestive of a scenario with two particle acceleration sites, the accreting binary remains the sole known source of power, meaning that any discussion about energetic requirements is unaffected. The existence of two acceleration sites is, however, considered when discussing constraints related to the morphology, as it effectively halves the distance that particles must travel to reproduce the observed extension. Figure 3 shows the prediction of the best-fit models in the leptonic and hadronic scenario, which are discussed in detail below.

6.2.1. Leptonic scenario

Relativistic electrons in low-density environments emit primarily via synchrotron and IC scattering. For relativistic electrons with Lorentz factor γ , the synchrotron loss time in a magnetic field with energy density $u_{\rm B}=B^2/8\pi$ is $\rm t_{syn}\propto (\gamma u_{\rm B})^{-1}$. For IC losses, the timescale is $\rm t_{IC}\propto (\gamma u_{\rm rad})^{-1}$, provided the Thomson regime applies, i.e. the typical target photon energy $\varepsilon_{\rm ph}$ satisfies $\gamma \varepsilon_{\rm ph} \ll mc^2$. Otherwise, Klein-Nishina suppression reduces the IC scattering rate, increasing the cooling time (see Figure 9).

To characterise the ambient radiation fields around V4641 Sgr, we used the combination of a publicly available axisymmetric Galactic model for the energy densities of the diffuse interstellar radiation field (Popescu et al. 2017) and the Cosmic Microwave Background (CMB). The total energy density of the target photons is $u_{\rm rad} = 2.2~{\rm eV~cm}^{-3}$. We ignored the radiation from the companion star in the binary system because its energy density is negligible across the size of the gamma-ray emitting region.

Spectra: Since the X-ray synchrotron flux depends on u_B , we could use the measurement by XRISM (Suzuki et al. 2025) to place an upper limit on the strength of the magnetic field. The short XRISM exposure was not sufficient to disentangle the nature of the X-ray emission (synchrotron or thermal emission) or to accurately measure its spectral index. Suzuki et al. (2025) provided two options for the X-ray spectra of the non-thermal emission: we combined both with a box between 1-12 keV ranging between $(1.6 - 3) \times 10^{-12}$ erg cm⁻² s⁻¹ (see Figure 8). We used this measurement as an upper limit to account for the possible thermal origin. The XRISM spectral extraction region is 629.4 arcmin² (Suzuki et al. 2025). We therefore scaled the measured flux to the 95% containment region of model A (1326 arcmin²). This approach is a priori conservative, since XRISM did not detect significant emission across the entirety of the gamma-ray emitting region that it covered, but only from a smaller region (see Figure B.1), suggesting that this upper limit could be lower. While there could in principle be bright X-ray emission outside of the XRISM FoV, analysis of archival *Chan*dra and XMM-Newton data with different coverage, partially covering regions outside the XRISM FoV, finds consistent flux measurements across the region (Suzuki et al. 2025). The combined Chandra, XMM-Newton and XRISM observations cover 75% of the gamma-ray emission region, defined as the spatial component of model A. Note that this estimate does not take into account differences in the acceptance across the FoV of the X-ray instruments.

We modelled a population of electrons with spectra which follows a power-law of index Γ_e with an exponential cut-off at $E_{\rm cut}$ (i.e. $\frac{dN_e}{dE_e} \propto E_e^{-\Gamma_e} \times \exp{(-\frac{E_e}{E_{\rm cut}^0})}$). Electrons were continuously injected for $t_{\rm inj}$, a time during which they lose energy due to interaction with assumed time-constant magnetic and radiation fields. The electron spectrum was normalised such that the integrated electron luminosity (above $E_{\rm min}^e = 1$ MeV) is some fraction α_e of the Eddington luminosity of the system ($L_{\rm Edd} \approx 10^{39}~{\rm erg~s^{-1}}$). The value of $t_{\rm inj}$ has a direct impact on the spectral shape of the gamma-ray emission: the longer $t_{\rm inj}$, the more photons are produced at low energies, as a consequence of the accumulation of low-energy electrons due to the energy-dependent loss timescale. This introduces a degeneracy between the spectral index and the assumed $t_{\rm inj}$: the hard spectral index detected by H.E.S.S. can be explained either with a low $t_{\rm inj}$ or a hard particle index. We perform the fit for several values of $t_{\rm inj}$ to assess the impact of this choice.

Owing to the computational cost of fitting the GAMERA model, we used a nested sampling algorithm (Skilling 2004) to explore the multi-dimensional likelihood function and find its minimum. This approach has the advantage that it also samples the posterior distributions of the parameters, providing a more accurate representation of errors and correlation between parameters. We used the sampling interface included in *Gammapy 2.0* (Donath et al. 2023; Acero et al. 2024), which derives posterior probability distributions and Bayesian evidence values through the nested sampling Monte Carlo algorithm MLFriends (Buchner 2016, 2019) using the UltraNest⁶ package (Buchner 2019).

The best-fit values for different $t_{\rm inj}$ are shown in Table 2. The parameters α_e , Γ_e and $E_{\rm cut}^e$ are highly correlated and as a consequence their posterior distributions cannot be described as Gaussian. For this reason, we provide the 68 and 95% containment intervals (C.I.) for each of the fitted parameters to more accurately represent their range of validity.

⁶https://johannesbuchner.github.io/UltraNest/

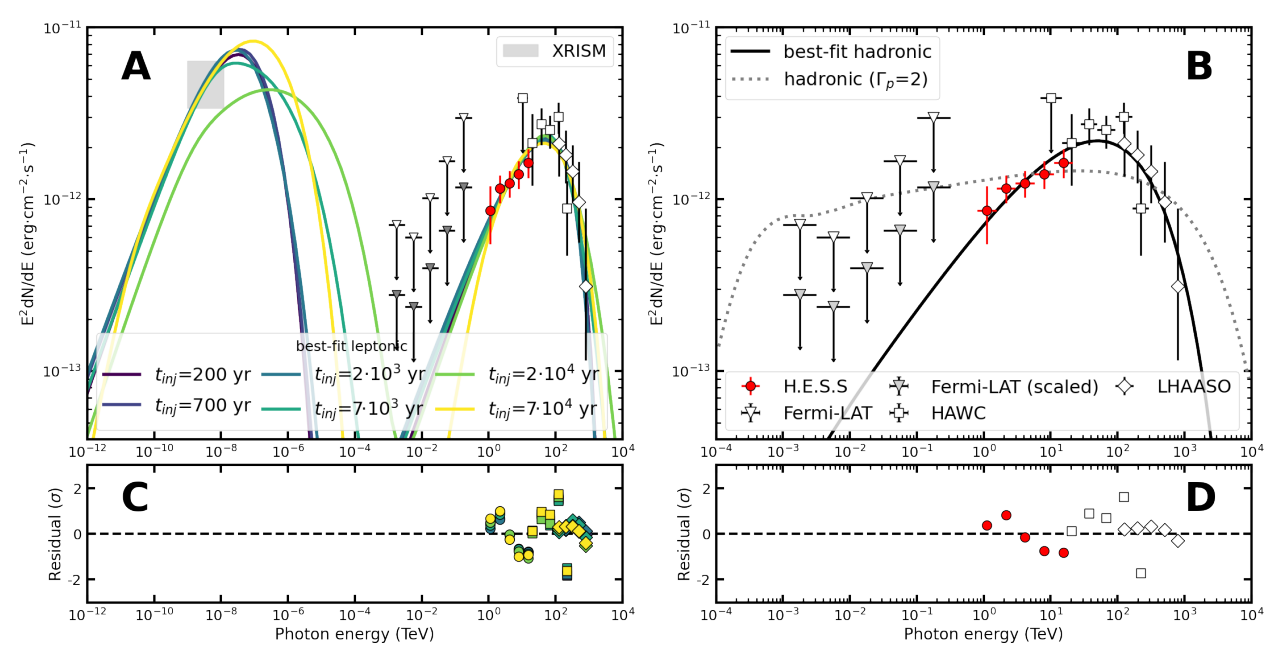


Fig. 8. Multi-wavelength SED and best-fit single-zones models. *Panel A:* The flux points and upper limits follow those of Figure 3. The XRISM flux region (scaled to the H.E.S.S. emission region size) is depicted with a grey shaded region. The *Fermi*-LAT points are shown both as published in Zhao et al. (2025) (light triangles) and re-scaled to the H.E.S.S. emission region size (dark triangles). The solid lines show the prediction of the best-fit leptonic model for different assumptions of t_{inj} . *Panel B:* The flux point symbols follow those of panel A. The black solid line shows the prediction of the best-fit hadronic model. The model obtained by fitting with a fixed $\Gamma_p = 2$ is shown with a grey dotted line for reference. *Panels C and D:* The residuals between the data and the best-fit models. In the leptonic case, colours indicate the model and symbols the dataset.

Regardless of the assumption of $t_{\rm inj}$, we found that the average magnetic field strength B is $< 5~\mu G$ in all cases, with the best-fit values ranging between 2-3 μG . These values of B should be interpreted as upper limits for a leptonic model, as we are assuming that the XRISM emission is entirely non-thermal and extends across the entire gamma-ray emission region. The obtained values of B are an order of magnitude lower than the estimate for the jets of SS 433 (H.E.S.S. Collaboration et al. 2024), which is the only other TeV microquasar for which the magnetic field strength has been estimated via a combined X-ray and gamma-ray fit.

While we are not able to distinguish statistically between the different $t_{\rm ini}$ considered (the largest $\Delta TS < 2$), we can make physical arguments to constrain this parameter. Relatively high values of $t_{\rm inj}$ require either an extremely hard (Γ_e < 1) particle spectral index or high $(E_{\text{cut}}^e > 10 \text{ PeV})$ cut-off energy to explain the observed gamma-ray spectrum. For $t_{\rm inj} \gtrsim 10^4$ yr the likelihood surface begins to display two minima, each corresponding to one of these two scenarios. We chose to include in Table 2 an example of each with the $t_{\rm inj} = 2 \times 10^4$ and $t_{\rm inj} = 7 \times 10^4$ yr cases. While in principle such a hard spectral index or high-energy cutoff are not excluded, a scenario with $\Gamma_e \approx 2$ and $E_{\text{cut}}^e \approx \text{few PeV}$ is closer aligned with theoretical expectations for particle acceleration, and thus we interpret our results to tentatively suggest $t_{\rm inj} \lesssim 10$ kyr. Additionally, the preferred equipartition ratio of magnetic to electron energy density (which should be interpreted as an upper limit) is less than one for high values of t_{ini} (see Table 2), which further disfavours such a scenario. Conversely, scenarios with a low $t_{\rm inj}$ require > 1% of the Eddington luminosity to be injected into the electron population on average, a requirement which relaxes as $t_{\rm inj}$ increases. The resulting equipartition ratio in this case is greater than one for t_{inj} less than a few thousand years. Consequently, we suggest that t_{inj} is likely in the 1-10 kyr range, but note that this estimate is subject to several

assumptions and thus uncertain. For $t_{\rm inj}$ in that range, we derive a lower limit on $E_{\rm cut}^e$ of ≈ 0.5 PeV (95% C.L.), with best-fit values around 1 PeV, with the caveat that this parameter is highly dependent on the particle index and thus the assumption of $t_{\rm ini}$.

Morphology. The energy-dependent loss timescale of electrons often equates to an energy-dependent morphology of the resulting emission (e.g. H.E.S.S. Collaboration et al. 2019, 2024). In particular, since the target radiation fields are isotropic and close to homogeneous on the spatial scales of interest, the morphology seen in IC gamma rays reflects the combined action of cooling and particle transport, the latter also being energy-dependent. In the absence of a significantly energy-dependent morphology, two options are possible: either the combination of transport and energy loss is energy independent or energy-independent transport is faster than energy loss. Figure 9 shows the relevant timescales as a function of energy. In order for a leptonic scenario to match the observed morphology, electrons must travel large enough distances without significant cooling. As shown in Figure 9, synchrotron emission is the dominant loss mechanism for electron energies greater than 10 TeV, meaning that higherenergy particles lose energy faster than low-energy ones. In particular, for magnetic field strengths of 5 and 3 μ G (motivated by the containment intervals reported in Table 2) the energy loss times of a 1 PeV electron are respectively 500 and 1300 yr.

If the jets are indeed aligned with the line of sight, transport out to large scales - in the special environment - would need to be diffusion-dominated, with the elongated morphology requiring the existence of a reasonably ordered large-scale magnetic field. The spatial extent of the emission can be governed by either cooling losses or by the extent of the "special environment" itself. In the first case, energy-dependent cooling and energy-dependent diffusion must conspire to avoid an energy-dependent morphology. In the second case, it is suffi-

Table 2. Best-fit values and confidence intervals (C.I.) for the parameters of the hadronic and a selection of the leptonic spectral models.

Parameter	Best-fit value	68% C.I.	95% C.I.
leptor	nic model, $t_{inj} =$	$2 \times 10^2 \text{ yr}$	
$B(\mu G)$	2.72	(2.11, 3.26)	(1.31, 3.82)
α_e (% of L _{Edd})	2.13	(1.45, 5.13)	(1.10, 8.59)
Γ_e	1.85	(1.70, 2.01)	(1.47, 2.07)
E_{cut}^{e} (PeV)	0.49	(0.33, 0.86)	(0.21, 1.46)
u_{tot}^{e} (eV cm ⁻³)	0.08	(0.06, 0.20)	(0.04, 0.33)
u_B/u_{tot}^e	2.22	-	-
leptor	nic model, $t_{\rm inj} =$	$2 \times 10^3 \text{ yr}$	
$B(\mu G)$	2.87	(2.26, 3.45)	(1.48, 3.96)
α_e (% of L _{Edd})	0.33	(0.20, 1.41)	(0.13, 3.52)
Γ_e	1.93	(1.82, 2.12)	(1.59, 2.19)
$E_{\rm cut}^e ({\rm PeV})$	0.99	(0.59, 11.59)	(0.31, 68.41)
u_{tot}^e (eV cm ⁻³)	0.13	(0.08, 0.55)	(0.05, 1.37)
u_B/u_{tot}^e	1.59	-	-
leptor	nic model, $t_{inj} =$	$2 \times 10^4 \text{ yr}$	
$B(\mu G)$	1.91	(1.54, 2.66)	(1.1, 3.5)
α_e (% of L _{Edd})	0.04	(0.03, 0.06)	(0.02, 0.1)
Γ_e	1.81	(1.59, 1.87)	(1.39, 1.98)
E_{cut}^{e} (PeV)	20.31	(2.58, 49.09)	(0.88, 90.95)
u_{tot}^{e} (eV cm ⁻³)	0.16	(0.12, 0.23)	(0.08, 0.39)
u_B/u_{tot}^e	0.58	-	-
leptor	nic model, $t_{\rm inj} =$	$7 \times 10^4 \text{ yr}$	
$B(\mu G)$	2.84	(2.11, 3.42)	(1.4, 3.99)
α_e (% of L _{Edd})	0.03	(0.02, 0.09)	(0.01, 0.19)
Γ_e	<1.0	(1.0, 1.43)	(1.0, 1.62)
E_{cut}^{e} (PeV)	1.74	(1.45, 28.2)	(1.16, 78.09)
u_{tot}^{e} (eV cm ⁻³)	0.41	(0.27, 1.22)	(0.14, 2.58)
u_B/u_{tot}^e	0.49	-	-
	hadronic mod	lel	
$ \frac{\Gamma_{p}}{E_{tot}^{p}(10^{50}\times n_{0.2\ cm^{-3}}^{-1}\ erg)} u_{tot}^{p}(n_{0.2\ cm^{-3}}^{-1}\ keV\ cm^{-3}) $	1.49	(1.24, 1.64)	(1.04, 1.79)
$E_{tot}^p(10^{50}\times n_{0.2~cm^{-3}}^{-1} \text{ erg})$	8.0	(7.17, 8.76)	(6.57, 10.31)
$u_{tot}^{p} (n_{0.2 \text{ cm}^{-3}}^{-1} \text{ keV cm}^{-3})$	0.49	(0.44, 0.54)	(0.40, 0.63)
$E_{\text{cut}}^{p} (\text{PeV})$	1.74	(1.00, 2.69)	(0.72, 4.99)

Notes. The normalisation parameter α_e is given as a percentage of $L_{\rm Edd}$ and not fraction. The energy densities of protons (u^p_{tot}) and electrons (u^p_{tot}) assume a cylindrical geometry, but we note that the depth of the emission region is completely unconstrained. Cooling and escape were ignored when deriving the energy densities. The magnetic field strengths should be interpreted as upper limits (see the discussion in the text) and, consequently, also the derived equipartition ratio u_B/u^e_{tot} .

cient that cooling is slow enough to reach the edge of the "special environment" without significant losses. We can estimate how fast diffusion must operate in the cooling-limited case by taking $r_1 \approx \sqrt{2 \times D(E) \times t_{cool}(E)}$, which for 1 PeV results in $D_{1\ PeV} = (2.8-7.6) \times 10^{29}\ \mathrm{cm^2\ s^{-1}}$ for the range of magnetic field strengths considered. These diffusion coefficients are ≈ 25 and 100 times larger than the Bohm diffusion coefficient at the same energy and value of B and roughly one order of magnitude lower than the Galactic average value, consistent with estimates derived from observations of other gamma-ray sources (e.g. Abeysekara et al. 2017).

The lack of observed energy dependence in the gamma-ray morphology between photon energies of 1 and 100 TeV also imposes constraints on the energy dependence of diffusive transport in the cooling-limited case. Adopting a diffusion coefficient $D(E) \propto E^{\delta}$, and cooling time $t_{cool}(E) \propto E^{-\gamma}$, we can write $r_1(E) \propto E^{0.5(\delta-\gamma)}$. The ratio between r_1 for a difference of

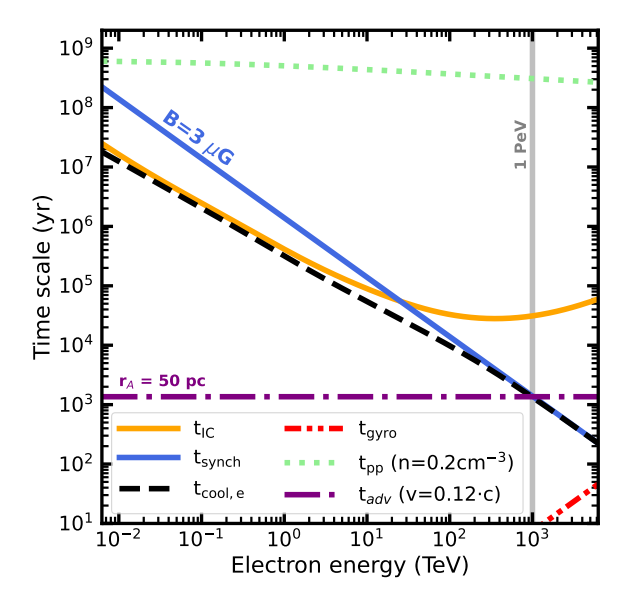


Fig. 9. Relevant timescales. The cooling timescale as a function of electron energy (black dashed line) assuming $B=3~\mu G$ and the same ambient radiation field as used in the broadband modelling. The contributions from IC and synchrotron are shown in orange and blue, respectively. The loss timescale of proton-proton interactions (Kafexhiu et al. 2014) is depicted with a dotted green line for density values of n= $0.2~\rm cm^{-3}$. A solid vertical line indicates 1 PeV particle energy. The purple dashed-dotted line indicates the propagation time of a flow moving with v=0.12c, over 50 pc. The red dashed-double-dotted line shows the gyro-radius time defined as $t_{\rm gyro}=2\pi r_g/c$ where r_g is the particle gyro-radius for $B=3~\mu G$. For n= $0.2~\rm cm^{-3}$ the bremsstrahlung loss timescale is $\approx 10^8~\rm yr$, and thus only relevant for energies lower than those shown in this figure.

roughly two orders of magnitude in electron energy would then be $10^{\delta-\gamma}$. Conservatively requiring that r_1 does not change by more than a factor 2 in this energy range requires $|\delta-\gamma|<0.3$. Figure 9 shows that for electron energies in the relevant range (\approx 4-400 TeV), the cooling time has a slope $\gamma \approx \frac{3}{4}$, which requires $0.45 \lesssim \delta \lesssim 1.05$. This constraint is dependent on the magnetic field strength, which could be even lower. For example if $B=1~\mu\text{G}$, IC would be the dominant cooling mechanism for electron energies slightly below 1 PeV, translating to a lower γ which in turn constrains δ to a narrower range. Note that this estimate assumes that the emission region size is limited by cooling and not the extent of the special environment.

In the hidden jets scenario, a natural transport mechanism would be advection with the jet flow. Advection is energy-independent, so in order to avoid energydependent morphology along the jets like in the case of SS 433 (H.E.S.S. Collaboration et al. 2024), advection must be faster than the energy loss timescale. This places a constraint $v > r_1/t_{cool} = 0.12 \times (\sin \phi)^{-1} c$ for $B = 3 \mu G$ and $v > r_1/t_{cool} =$ $0.33 \times (\sin \phi)^{-1} c$ for $B = 5 \mu G$, where ϕ would be the jet inclination angle. Consequently, even assuming a relatively high magnetic field, this hypothetical advection speed would only need to be mildly relativistic to account for the observed gamma-ray morphology. The reported jet velocity of V4641 Sgr is highly relativistic, but that is of course only relevant to the jet with a low inclination angle, which would not be consistent with the observed gamma-ray morphology. If the advection flow is indeed much faster than the constraints above and does not significantly decelerate, the emission region size would not be determined by cooling losses but instead it should be explained by the intrinsic

size of the jets and/or their cocoon (see Equation 1). If we consider the situation where acceleration occurs at a point further along the jets (site 2; see Figure 7), the fact that there is significant gamma-ray emission in the region between the model centroids (see e.g. Figure 4) rules out a pure advection model in that scenario. We cannot rule out that electrons might be accelerated at site 2, however, and instead of being advected further, they diffuse outwards from these locations. In that case the relevant spatial scale is r_2 , and thus the diffusion coefficient would be a factor of 2 smaller than the values in the paragraphs above.

While low magnetic field strengths ease energy losses in the leptonic scenario, they pose a challenge for accelerating particles to PeV energies. Assuming a single-zone configuration, in which the particle acceleration and emission occur under the same ambient conditions, following Hillas (1984), we infer a maximum energy of

$$E_{\rm Hillas} \approx 3.5 Z \left(\frac{B}{3\mu \rm G}\right) \left(\frac{v_{\rm jet}}{c}\right) \left(\frac{R}{1 \rm pc}\right) \rm PeV,$$
 (2)

where R is the extent of the acceleration region. For $v_{\rm jet}=c$, that is, optimal acceleration conditions, an accelerator of $R\approx 1$ pc could produce 3.5 PeV electrons (in the absence of losses). For even lower magnetic field values (e.g. $B=1~\mu{\rm G}$), this optimal accelerator would need to be larger than 1 pc to produce 1 PeV electrons. While these are extreme conditions, the acceleration sites in the jets of the microquasar SS 433 have been estimated to be $\approx 1-2$ pc (H.E.S.S. Collaboration et al. 2024; Safi-Harb et al. 2022; Kayama et al. 2022). There is a precedent for highly efficient acceleration in the Crab nebula (LHAASO Collaboration et al. 2021). Alternatively, there could also be a two-zone configuration, where particles are accelerated in a smaller region with a higher magnetic field, but manage to escape fast enough to a second zone where losses are less severe (e.g. Breuhaus et al. 2021).

6.2.2. Hadronic scenario

If protons are accelerated to relativistic energies somewhere in the V4641 Sgr system, they can produce gamma-ray radiation through inelastic collisions with nearby gas (pp-interactions). As the energy dependence of the pp cross-section far above threshold is approximately logarithmic, the energy loss timescale of protons has a weak energy dependence, as shown in Figure 9. The main parameter governing this process is the ambient density n_{gas} , to which the energy loss rate is directly proportional. Conversely, the magnetic field strength is not well constrained in a hadronic scenario. Energy conservation limits the total energy emitted via synchrotron radiation from secondary electrons produced by decaying charged pions to not exceed that of the gamma rays. Unfortunately, the XRISM X-ray flux bounds are not sufficiently constraining, as they are higher than the measured gamma-ray flux.

Spectra. We fitted the spectrum resulting from pp-interactions of a population of protons distributed following a power-law spectrum with an exponential cut-off: $\frac{dN_p}{dE_p} \propto E_p^{-\Gamma_p} \times \exp{(-\frac{E_p}{E_{\rm cut}^p})}$. As with the electrons, we normalised this power-law such that the integrated proton luminosity (above $E_{\rm min}^p = 1$ GeV) is some fraction α_p of the Eddington luminosity of the system (L_{Edd}). The value of α_p required to match the gamma-ray flux is inversely proportional to the value of $n_{\rm gas}$. We assumed that protons are injected continuously for $t_{\rm inj}$, where the only constraint

on this time is that $t_{\rm inj} \lesssim 2$ Myr (Salvesen & Pokawanvit 2020). In order to avoid introducing further uncertainty, we discuss the proton normalisation in terms of the total energy, defined as $E_{\rm tot}^p = \alpha_p \times L_{\rm Edd} \times t_{\rm inj}$ and simply note that the gamma-ray emission could require a higher or lower fraction of the jet luminosity depending on the assumed $t_{\rm inj}$.

We fitted the photon spectrum calculated with GAMERA using the same framework and gamma-ray data points as in the leptonic scenario. We found best-fit values for the index, cutoff energy and total energy of $\Gamma_p=1.49$, $E_{\rm cut}^p=1.74$ PeV and $E_{\rm tot}^p=8\times 10^{50}\times {\rm n}_{0.2~cm^{-3}}^{-1}$ erg, respectively. The 68 and 95% containment intervals for each parameter are provided in Table 2. The best-fit spectrum is shown in panel B of Figure 8 together with the measured flux points and upper limits. The cut-off energy is only weakly constrained towards higher energies, with $E_{\rm cut}^p \lesssim 5~{\rm PeV}$ (99% containment limit). A particle index $\Gamma_p=2$ can be rejected with 5σ certainty, as a hard particle spectrum is required by the spectral index measured with H.E.S.S. and is consistent with the non-detection in the GeV band. It is generally thought that shock acceleration produces flat spectra with indeces in the 2-2.2 range (Drury 1983) and while spectra as hard as 1.5 are theoretically possible (Kirk & Heavens 1989; Malkov 1999; Summerlin & Baring 2012), they require extreme conditions or fine-tuning. Figure 8 also shows the best-fit spectra obtained when fixing Γ_p to a value of 2. In this case, the required E_{cut}^p increases by almost an order of magnitude and the emission over-predicts significantly the GeV range while failing to describe the measured gamma-ray flux points.

The above energetic requirements pose a challenge for the hadronic scenario. As detailed in Section 5 and Appendix C, there is no observed gas structure with a morphology resembling that of the gamma-ray emission (at any distance, or even combining all distances). The average density on the scale of the gamma-ray emission is $n_{\rm gas} < 0.2~{\rm cm}^{-3}$, translating to $E_{tot}^p > 8 \times 10^{50}$ erg. If an average of $\approx 10\%$ of the jet power was injected as energetic protons, and the jet operated at $L_{\rm Edd}$ for $\approx 10\%$ of the time ($\alpha_p \times \eta_{\rm jet} = 0.01$), this process would need to be operating at this level for a minimum of 2.5 Myr. During this time, the source would have moved more than one degree in the sky (Salvesen & Pokawanvit 2020). Consequently, providing the observed gamma-ray flux requires extraordinarily efficient conditions.

Morphology. The gamma-ray morphology in the hadronic scenario results from both the particles' spatial distribution and the shape of the target gas. As shown in Section 5, there is no dense gas structure matching the observed gamma-ray morphology, which implies that its asymmetry would be the product of asymmetric transport. In the special environment scenario, having ruled out the presence of a matching molecular cloud, diffusion would need to be anisotropic and almost energy independent ($\delta \gtrsim 0$) in order to avoid resulting in observable energy-dependent morphology.

Approximating the gamma-ray emission as a cylinder of radius 10 pc and height 110 pc results in a particle energy density of $u_{tot}^p > 0.5 \text{ keV} \cdot \text{cm}^{-3}$. Typical ISM conditions (Ferrière 2001) can not confine such energy densities. The protons might still be confined in a cocoon inflated by the jets, however. In this scenario, the morphology would be determined by the size of the cocoon, which follows Equation 1. This also requires that the proton confinement time, t_{conf} must be much greater than t_{jet} , which in turn would be $t_{\text{jet}} \gtrsim t_{\text{inj}}$. Consequently, the jets would need to provide sufficiently strong magnetic fields to couple the

particles to the cocoon material. Assuming equipartition with the protons gives $B=100\,\mu\text{G}$. A strict upper bound to the confinement time in the cocoon is then given by the Bohm limit $(D>D_{\text{Bohm}}, \text{e.g. Aharonian (2004)})$:

$$t_{\rm conf} < \frac{R_c^2}{4D_{\rm Bohm}} \approx 500 \left(\frac{R_c}{50\,{\rm pc}}\right)^2 \left(\frac{E}{{\rm PeV}}\right)^{-1} \left(\frac{B}{100\,\mu{\rm G}}\right) {\rm kyr}$$
 (3)

where $R_c \approx \ell_c/2$ is half the system size. While in principle the requirement $t_{\rm conf} \gg t_{\rm jet}$ can be fulfilled if, for example, the value of $v_{\rm jet}$ in Equation 1 was lower or $\eta_{\rm jet}$ higher, a cocoon scenario would also imply even lower gas densities within the jet cavity. This in turn, exacerbates the extreme energy requirements described above, especially if the jet is only active for hundreds of kyr, which requires $\alpha_p \times \eta_{\rm jet} \gtrsim 0.1$.

We conclude that a hadronic origin of the gamma-ray emission is unlikely. In such a low-density environment, not observing hadronic emission does not negate the existence of accelerated hadrons.

7. Conclusions

We have presented a detailed study of the gamma-ray emission around V4641 Sgr, including physical modelling for a leptonic and a hadronic scenario. We reached a number of conclusions that we list below.

- The gamma-ray emission is highly elongated, with 68% containment diameters of about 110d_{6.2kpc} and 20d_{6.2kpc} pc in either direction. The direction of this elongation disagrees with the proper motions of the source and with any other known intrinsic direction in the system.
- The gamma-ray morphology shows weak evidence for two components. This is preferred by 3σ over a model with a single elongated component. In any case, the spectra are consistent throughout the entire emission region, with a photon spectral index of $\Gamma \approx 1.8$.
- The spectral index measured by the H.E.S.S. data implies a rising spectral energy distribution in the 1-20 TeV range. HAWC and LHAASO data then show a turnover at energies around 100 TeV. The data reveal a source spectrum that peaks at energies as high as ≈100 TeV for the first time.
- We found no evidence of an energy-dependent morphology in the 1-100 TeV energy range. Our comparison of the size of the emission across the major axis between H.E.S.S. and HAWC at several energies (Alfaro et al. 2024) showed consistency well within 1σ across two orders of magnitude in energy. The size appears to increase above 100 TeV, but it remains consistent within the 2.5σ uncertainties. Energy-dependent size measurements by the LHAASO Observatory at and above 100 TeV should be able to reveal whether this increase is real or simply a statistical fluctuation.
- A leptonic scenario can explain the observed spectra if the magnetic field strength is $B < 3 \mu G$. The timescale of the electron injection is not known and affects some of the best-fit parameters. We argued that $t_{\rm inj}$ is likely in the 1-10 kyr range by applying a number of assumptions. In this case, electrons above 1 MeV would require significantly less than 1% of $L_{\rm Edd}$ to match the observed gamma-ray flux, with $E_{\rm cut}^e$ slightly below 1 PeV.
- In the leptonic scenario, transport would need to be sufficiently fast for particles to cover dozens of pc without significant energy losses. We found that a hypothetical jet that

is not aligned with the line of sight would only need to be mildly relativistic ($v_{jet} \gtrsim 0.1c$) to allow for this. If transport were instead dominated by diffusion, the elongated morphology would require a highly ordered weak magnetic field structure around the source. The lack of a strongly energy-dependent morphology constrains the energy dependence of the cooling-limited diffusive transport $D(E) \propto E^{\delta}$ to $0.45 \lesssim \delta \lesssim 1.05$.

- Acceleration of ≈ 1 PeV electrons in an environment with such a low magnetic field is possible, but requires highly efficient acceleration and a relatively large (parsec-scale) acceleration site. These constraints would favour an acceleration site along the hypothetical jets, like in SS 433 (Safi-Harb et al. 2022; Kayama et al. 2022; H.E.S.S. Collaboration et al. 2024). Alternatively, electrons might be accelerated in a different region and be quickly transported to a region with a lower magnetic field.
- Dedicated radio observations of the region and publicly available observations constrain the average ambient gas density to be low, with $n_{gas} < 0.2 \text{ cm}^{-3}$. Lower values are found for neutral hydrogen.
- A hadronic scenario with a cut-off energy of about 2 PeV can reproduce the observed spectra, but only with an unusually hard (Γ_p=1.5) proton spectral index and with a strong requirement for the proton power, given the low ambient density. In particular, we found that the gamma-ray flux requires the proton energy above 1 GeV to be $E_{tot}^p \gtrsim 8 \times 10^{50}$ erg, which corresponds to an energy density $u_{tot}^p \gtrsim 0.5$ keV·cm⁻³. These numbers require at least 10% of the average jet power of a jet, with a 10% Eddington duty cycle being provided to protons for 2.5 Myr. This is the entire time for which the source is thought to have been at its current location (Salvesen & Pokawanvit 2020).
- The high proton energy density requires extreme properties $(B>100~\mu\mathrm{G})$ in order for the protons to remain confined in the gamma-ray-emitting volume long enough for the energy to accumulate. Given the distance of V4641 Sgr to the Galactic plane and the lack of observational evidence for an unusual environment, these conditions require something other than the normal ISM. We considered a jet cocoon scenario, but found that in order to describe the observations, finetuning and extreme energetic requirements were imposed.
- Because of these constraints, we conclude that the emission is most likely of leptonic origin. We propose the existence of a previously unknown large-scale outflow (hidden jet) aligned with the gamma-ray elongation axis, although a scenario with a highly ordered magnetic field structure (special environment) is also possible.
- The observed elliptic morphology in the single and double component scenarios requires that regardless of the dominant emission process, particle transport must be inherently anisotropic, with a preferred direction along the major axis of the gamma-ray emission. At the same time, the observed asymmetry of the emission with respect to the position of V4641 Sgr requires either an intrinsic warping or distortion of the jets and their cocoon or a specific magnetic topology that breaks the symmetry.
- Our statement that the gamma-ray emission is most likely of leptonic origin does not imply that V4641 Sgr is not a hadronic accelerator. Standard acceleration mechanisms do not distinguish between particles of different nature: If electrons are accelerated to energies above 1 PeV, protons might be as well.

- In either scenario, the observed gamma-ray flux implies a luminosity of $L_{\gamma} \approx 5 \times 10^{34} \text{ erg s}^{-1}$, which is hard to reconcile with the current luminosity of the system in other bands. Unlike SS 433, which is known to have been in a super-Eddington accretion regime since its discovery, the only instance where the output of V4641 Sgr was thought to have reached Eddington levels is the 1999 outburst. Since then, the source has been comparatively quiet, with only smaller outbursts with average luminosities of $\approx 10^{36}$ erg s⁻¹. For example, during the 2020 outburst, the luminosity was estimated to be lower by about an order of magnitude than $L_{\rm Edd}$ even when obscuration was accounted for (Shaw et al. 2022). The presence of bright extended gamma-ray emission on these spatial scales and the inferred maximum particle energies require that the system must have been consistently more active in the past (e.g. Peretti et al. 2025; Wang et al. 2025). While details depend on the scenario, the duration of this phase in the leptonic case with increased activity would need to be a few thousand years, while in the hadronic case, it would require timescales on the order of millions of years. This might exceed the thermal timescale of the companion star.

While the H.E.S.S. observations (combined with those of Fermi-LAT, HAWC, and LHAASO) provide constraints on the physics that cause the emission around V4641 Sgr, many questions remain. Upcoming X-ray observations with Chandra⁷, XMM-*Newton*, and *NuSTAR*⁸ will cover the entire gamma-ray emission region and will help us address some of them. For example, the X-ray observations will potentially further validate the leptonic interpretation because detectable X-ray emission is expected if $B > 1 \mu G$. Additionally, in analogy with SS 433 (Safi-Harb et al. 2022; Kayama et al. 2022), the superior angular resolution of X-ray instruments will be critical to constrain the location and nature of acceleration sites. Similarly, observations of the region with radio telescopes such as MeerKAT (Jonas 2018) or the future Square Kilometre Array Observatory (Braun et al. 2015) might provide a definite answer to the question of the jet geometry. In particular, recent radio campaigns have revealed the previously unknown large physical extent of jets originating in several X-ray binaries (e.g. Wood et al. 2024; Motta et al. 2025). Radio observations and a characterisation of the outflows from V4641 Sgr would provide much needed clarity on the geometry of the system.

Observing V4641 Sgr with future gamma-ray experiments such as the Cherenoky Telescope Array Observatory (CTAO) (Cherenkov Telescope Array Consortium et al. 2019) or the Southern Wide-field Gamma-ray Observatory (SWGO) (SWGO Collaboration et al. 2025) will also provide critical constraints. In particular, SWGO will be able to significantly improve the characterisation of the spectrum at the highest photon energies because V4641 Sgr will transit overhead at the SWGO site, but only reaches the edge of the HAWC and LHAASO FoVs. Complementarily, the dramatic improvement in angular resolution that CTAO will provide at energies of dozens of TeV (Schwefer et al. 2024) will bridge the gap between the current H.E.S.S. and HAWC/LHAASO morphological studies and either detect a weak energy-dependent morphology in the gamma-ray emission or rule it out entirely.

V4641 Sgr was the second microquasar detected at energies above the TeV range, and similar to the first, SS 433, a leptonic origin for the emission appears to be strongly preferred. The precessing jets of SS 433 are known to contain heavy nuclei (e.g. Migliari et al. 2002), however, and evidence for heavy nuclei in the jet of V4641 Sgr has also been reported (e.g. in't Zand et al. 2000). There is no reason to expect that these particles are excluded from the acceleration process. While microquasars remain one of the most compelling candidates to account for multi-PeV Galactic cosmic rays, direct evidence of hadronic emission from these systems is still lacking. Given the sensitivity of current neutrino detectors (Neronov et al. 2025), the most promising avenue remains the detection of gamma-ray emission coincident with dense gas near a microquasar. While the location of V4641 Sgr in the Galaxy facilitates its association with the gamma-ray emission, the low-density environment would also hide evidence of hadronic acceleration. It is thus required to observe and detect emission from other microquasars in different environments, with the caveat that the source identification becomes difficult in crowded Galactic regions. One such promising example is the microquasar GRS 1915+105, which is located in a relatively dense region and from which GeV and TeV emission have recently been reported (Martí-Devesa & Olivera-Nieto 2025; LHAASO Collaboration 2024b). GRS 1915+105 is located in the Galactic plane nearby many putative gamma-ray sources, however, and a detailed study of the emission and its origin therefore likely requires observations with an improved angular resolution, such as that of the upcoming CTAO.

The gamma-ray emission around V4641 Sgr is bright and persistent. It was detected by the HAWC Observatory as soon as improved algorithms expanded the HAWC FoV to include higher zenith angle ranges (Albert et al. 2024). While V4641 Sgr is only narrowly visible from the northern hemisphere, it transits almost overhead at the H.E.S.S. site. The region was still observed by H.E.S.S. for less than 10 h prior to the HAWC detection, which highlights the biases of pointed observations and the complementarity of IACTs and WCD arrays. Other sources like it may exist, but are simply located in poorly observed regions of the southern sky. This possibility would affect the expected contribution of microquasars to the cosmic-ray flux at petaelectronvolt energies. Additionally, the detection of emission surrounding V4641 Sgr and other jetted X-ray binaries (LHAASO Collaboration 2024b) firmly establishes microquasars as a class of gamma-ray emitters. These findings require a re-evaluation of the nature of unidentified gamma-ray sources, some of which might be connected to a previously disregarded X-ray binary.

Data availability: The map shown in Figure 1 is available in electronic form at the CDS via anonymous ftp to cdsarc.u-strasbg.fr (130.79.128.5) or via http://cdsweb.u-strasbg.fr/cgi-bin/qcat?J/A+A/. Further data products, such as machine-readable versions of the flux points and models discussed in the paper are provided via Zenodo (H.E.S.S. Collaboration 2025).

Acknowledgements. We thank Hiromasa Suzuki for providing the XRISM image. The support of the Namibian authorities and of the University of Namibia in facilitating the construction and operation of H.E.S.S. is gratefully acknowledged, as is the support by the German Ministry for Education and Research (BMBF), the Max Planck Society, the Helmholtz Association, the French Ministry of Higher Education, Research and Innovation, the Centre National de la Recherche Scientifique (CNRS/IN2P3 and CNRS/INSU), the Commissariat à l'énergie atomique et aux énergies alternatives (CEA), the U.K. Science and Technology Facilities Council (STFC), the Polish Ministry of Education and Science, agreement no. 2021/WK/06, the South African Department of Science and Innovation and National Research Foundation, the University of Namibia, the National Commission on Research, Science and Technology of Namibia (NCRST), the Austrian Federal Ministry of Education, Science and Research

⁷https://cxc.cfa.harvard.edu/target_lists/cycle27/ cycle27_approved_peer_targets_by_radec.html

⁸https://heasarc.gsfc.nasa.gov/docs/nustar/ao11/ c11_acceptarg.html

and the Austrian Science Fund (FWF), the Australian Research Council (ARC), the Japan Society for the Promotion of Science, the University of Amsterdam and the Science Committee of Armenia grant 21AG-1C085. We appreciate the excellent work of the technical support staff in Berlin, Zeuthen, Heidelberg, Palaiseau, Paris, Saclay, Tübingen and in Namibia in the construction and operation of the equipment. This work benefited from services provided by the H.E.S.S. Virtual Organisation, supported by the national resource providers of the EGI Federation. We are grateful to the staff of the Nobeyama Radio Observatory (NRO) for their outstanding support during the 45-m telescope observations. The NRO is a branch of the National Astronomical Observatory of Japan (NAOJ), National Institutes of Natural Sciences.

References

Aartsen, M. G., Ackermann, M., Adams, J., et al. 2019, Phys. Rev. D, 100, 082002

Abdo, A. A., Ackermann, M., Ajello, M., et al. 2010, ApJS, 187, 460 Abeysekara, A. U., Albert, A., Alfaro, R., et al. 2018, Nature, 562, 82

Abeysekara, A. U., Albert, A., Alfaro, R., et al. 2017, Science, 358, 911

Abeysekara, A. U., Archer, A., Benbow, W., et al. 2020, ApJ, 894, 51

Acero, F., Bernete, J., Biederbeck, N., et al. 2024, Gammapy: Python toolbox for gamma-ray astronomy

Aharonian, F. A. 2004, Very high energy cosmic gamma radiation: a crucial window on the extreme Universe (World Scientific Book)

Albert, A., Alfaro, R., Alvarez, C., et al. 2024, ApJ, 972, 144

Alfaro, R., Alvarez, C., Arteaga-Velázquez, J. C., et al. 2024, Nature, 634, 557

Amenomori, M., Bi, X. J., Chen, D., et al. 2008, ApJ, 678, 1165

Arimoto, N., Sofue, Y., & Tsujimoto, T. 1996, PASJ, 48, 275

Ashton, T., Backes, M., Balzer, A., et al. 2020, Astroparticle Physics, 118, 102425

Bailer-Jones, C. A. L., Rybizki, J., Fouesneau, M., Mantelet, G., & Andrae, R. 2018, AJ, 156, 58

Bao, Y., Giacinti, G., Liu, R.-Y., Zhang, H.-M., & Chen, Y. 2025, Phys. Rev. Lett., 135, 191002

Begelman, M. C. & Cioffi, D. F. 1989, ApJ, 345, L21

Bell, A. R. 2014, Brazilian Journal of Physics, 44, 415

Bi, B., Barcelo, M., Bauer, C., et al. 2022, in 37th International Cosmic Ray Conference. 12-23 July 2021. Berlin, 743

Blaauw, A. 1961, Bull. Astron. Inst. Netherlands, 15, 265

Blumenthal, G. R. & Gould, R. J. 1970, Reviews of Modern Physics, 42, 237 Bosch-Ramon, V., Aharonian, F. A., & Paredes, J. M. 2005a, A&A, 432, 609

Bosch-Ramon, V., Romero, G. E., & Paredes, J. M. 2005b, A&A, 429, 267

Brand, J. & Blitz, L. 1993, A&A, 275, 67

Braun, R., Bourke, T. L., Green, J. A., Keane, E., & Wagg, J. 2015, PoS, AASKA14, 174

Breuhaus, M., Hahn, J., Romoli, C., et al. 2021, ApJ, 908, L49

Buchner, J. 2016, Statistics and Computing, 26, 383

Buchner, J. 2019, PASP, 131, 108005

Cao, Z., Aharonian, F., An, Q., et al. 2024, ApJS, 271, 25

Cherenkov Telescope Array Consortium, Acharya, B. S., Agudo, I., et al. 2019, Science with the Cherenkov Telescope Array

Churazov, E., Khabibullin, I., Barnouin, T., et al. 2024, A&A, 686, A14 Cooper, A. J., Gaggero, D., Markoff, S., & Zhang, S. 2020, MNRAS, 493, 3212 CTA Consortium, Abe, S., Abhir, J., et al. 2024, J. Cosmology Astropart. Phys.,

Dame, T. M. & Thaddeus, P. 2022, ApJS, 262, 5

de Naurois, M. & Rolland, L. 2009, Astroparticle Physics, 32, 231

Díaz Trigo, M., Miller-Jones, J. C. A., Migliari, S., Broderick, J. W., & Tzioumis, T. 2013, Nature, 504, 260

Donath, A., Terrier, R., Remy, Q., et al. 2023, A&A, 678, A157

Drury, L. O. 1983, Reports on Progress in Physics, 46, 973

Ferrière, K. M. 2001, Reviews of Modern Physics, 73, 1031

Finkbeiner, D. P. 2003, ApJS, 146, 407

Gallo, E., Plotkin, R. M., & Jonker, P. G. 2014, MNRAS, 438, L41

Gandhi, P., Rao, A., Johnson, M. A. C., Paice, J. A., & Maccarone, T. J. 2019, MNRAS, 485, 2642

Gillessen, S. 2004, PhD thesis, Ruprecht-Karls-UniversitätHeidelberg

Ginzburg, V. L. & Syrovatskii, S. I. 1964, The Origin of Cosmic Rays (PERGA-MON PRESS)

Goranskij, V. P. 2001, Information Bulletin on Variable Stars, 5068, 1

Goranskij, V. P., Barsukova, E. A., & Burenkov, A. N. 2003, Astronomy Reports, 47,740

Hahn, J. 2015, in International Cosmic Ray Conference, Vol. 34, 34th International Cosmic Ray Conference (ICRC2015), 917

Hahn, J., Romoli, C., & Breuhaus, M. 2022, GAMERA: Source modeling in gamma astronomy, Astrophysics Source Code Library, record ascl:2203.007

H.E.S.S. Collaboration. 2025, Data files for "Constraining the nature of the most extreme Galactic particle accelerator: H.E.S.S. observations of the microquasar V4641 Sgr

H.E.S.S. Collaboration, Abdalla, H., Abramowski, A., et al. 2018a, A&A, 612, A10

H.E.S.S. Collaboration, Abdalla, H., Abramowski, A., et al. 2018b, A&A, 612,

H.E.S.S. Collaboration, Abdalla, H., Aharonian, F., et al. 2019, A&A, 621, A116 H.E.S.S. Collaboration, Aharonian, F., Ait Benkhali, F., et al. 2023, A&A, 672, A103

H.E.S.S. Collaboration, Aharonian, F., Ait Benkhali, F., et al. 2024, Science, 383, 402

H.E.S.S. Collaboration, Aharonian, F., Akhperjanian, A. G., et al. 2006, A&A, 457, 899

Heyer, M. & Dame, T. M. 2015, ARA&A, 53, 583

Hillas, A. M. 1984, ARA&A, 22, 425

Hillas, A. M. 1985, in International Cosmic Ray Conference, Vol. 3, 19th International Cosmic Ray Conference (ICRC19), Volume 3, 445

Hillas, A. M. 2005, Journal of Physics G Nuclear Physics, 31, R95

Hinton, J. A. & Hofmann, W. 2009, ARA&A, 47, 523

Hjellming, R. M., Rupen, M. P., Hunstead, R. W., et al. 2000, ApJ, 544, 977 Holler, M., Berge, D., van Eldik, C., et al. 2015, in International Cosmic Ray Conference, Vol. 34, 34th International Cosmic Ray Conference (ICRC2015), 847

in't Zand, J. J. M., Kuulkers, E., Bazzano, A., et al. 2000, A&A, 357, 520 Jonas, J. 2018, PoS, MeerKAT2016, 001

Kafexhiu, E., Aharonian, F., Taylor, A. M., & Vila, G. S. 2014, Phys. Rev. D, 90, 123014

Kalberla, P. M. W. & Haud, U. 2018, A&A, 619, A58

Kantzas, D., Markoff, S., Cooper, A. J., et al. 2023, MNRAS, 524, 1326

Kayama, K., Tanaka, T., Uchida, H., et al. 2022, Publications of the Astronomical Society of Japan, 74, 1143

Kirk, J. G. & Heavens, A. F. 1989, MNRAS, 239, 995

Langer, N., Deutschmann, A., Wellstein, S., & Höflich, P. 2000, A&A, 362, 1046 LHAASO Collaboration. 2024a, Science Bulletin, 69, 449

LHAASO Collaboration. 2024b, arXiv e-prints, arXiv:2410.08988

LHAASO Collaboration, Cao, Z., Aharonian, F., et al. 2021, Science, 373, 425 LHAASO Collaboration, Cao, Z., Aharonian, F., et al. 2025, arXiv e-prints, arXiv:2505.14447

MacDonald, R. K. D., Bailyn, C. D., Buxton, M., et al. 2014, ApJ, 784, 2 Malkov, M. A. 1999, ApJ, 511, L53

Margon, B., Ford, H. C., Grandi, S. A., & Stone, R. P. S. 1979, ApJ, 233, L63

Markoff, S., Nowak, M. A., & Wilms, J. 2005, ApJ, 635, 1203

Markwardt, C. B., Swank, J. H., & Marshall, F. E. 1999, IAU Circ., 7120, 1 Marshall, H. L., Canizares, C. R., & Schulz, N. S. 2002, ApJ, 564, 941

Martí-Devesa, G. & Olivera-Nieto, L. 2025, ApJ, 979, L40

Martin, R. G., Reis, R. C., & Pringle, J. E. 2008, MNRAS, 391, L15

Migliari, S., Fender, R., & Méndez, M. 2002, Science, 297, 1673

Miller, J. M., Fabian, A. C., in't Zand, J. J. M., et al. 2002, ApJ, 577, L15 Mohrmann, L., Specovius, A., Tiziani, D., et al. 2019, A&A, 632, A72

Motta, S. E., Atri, P., Matthews, J. H., et al. 2025, A&A, 696, A222

Muñoz-Darias, T., Torres, M. A. P., & Garcia, M. R. 2018, MNRAS, 479, 3987

Neronov, A., Oikonomou, F., & Semikoz, D. 2025, Phys. Rev. D, 111, 103025 Ohm, S., van Eldik, C., & Egberts, K. 2009, Astroparticle Physics, 31, 383

Orosz, J. A., Kuulkers, E., van der Klis, M., et al. 2001, ApJ, 555, 489

Parsons, R. D. & Hinton, J. A. 2014, Astroparticle Physics, 56, 26

Peretti, E., Petropoulou, M., Vasilopoulos, G., & Gabici, S. 2025, A&A

Pineda, J. L., Langer, W. D., Velusamy, T., & Goldsmith, P. F. 2013, A&A, 554, Planck Collaboration, Adam, R., Ade, P. A. R., et al. 2016, A&A, 594, A10

Podsiadlowski, P., Rappaport, S., & Pfahl, E. D. 2002, ApJ, 565, 1107 Popescu, C. C., Yang, R., Tuffs, R. J., et al. 2017, MNRAS, 470, 2539 Reid, M. J., Menten, K. M., Brunthaler, A., et al. 2019, ApJ, 885, 131 Revnivtsev, M., Gilfanov, M., Churazov, E., & Sunyaev, R. 2002a, A&A, 391, 1013

Revnivtsev, M., Sunyaev, R., Gilfanov, M., & Churazov, E. 2002b, A&A, 385, 904

Safi-Harb, S., Mac Intyre, B., Zhang, S., et al. 2022, ApJ, 935, 163 Salvesen, G. & Pokawanvit, S. 2020, MNRAS, 495, 2179

Schwefer, G., Parsons, R., & Hinton, J. 2024, Astroparticle Physics, 163, 103008 Shaw, A. W., Miller, J. M., Grinberg, V., et al. 2022, MNRAS, 516, 124

Skilling, J. 2004, in American Institute of Physics Conference Series, Vol. 735, Bayesian Inference and Maximum Entropy Methods in Science and Engineering: 24th International Workshop on Bayesian Inference and Maximum Entropy Methods in Science and Engineering, ed. R. Fischer, R. Preuss, & U. V. Toussaint (AIP), 395-405

Sofue, Y. 2015, PASJ, 67, 75

Summerlin, E. J. & Baring, M. G. 2012, ApJ, 745, 63

Suzuki, H., Tsuji, N., Kanemaru, Y., et al. 2025, ApJ, 978, L20

SWGO Collaboration, Abreu, P., Alfaro, R., et al. 2025, arXiv e-prints, arXiv:2506.01786

Tsuji, N., Takekawa, S., Mori, K., et al. 2025, ApJ, 983, 22 Unbehaun, T., Lang, R. G., Deka Baruah, A., et al. 2025, A&A, 694, A162 Wang, J., Reville, B., & Aharonian, F. A. 2025, ApJ, 989, L25 Wijnands, R. & van der Klis, M. 2000, ApJ, 528, L93

Winkel, B., Kerp, J., Flöer, L., et al. 2016, A&A, 585, A41

Wood, C. M., Miller-Jones, J. C. A., Bahramian, A., et al. 2024, ApJ, 971, L9 Zhao, Z., Li, J., & Torres, D. F. 2025, ApJ, 984, 3

- ¹ University of Southern Denmark
- ² Astronomy & Astrophysics Section, School of Cosmic Physics, Dublin Institute for Advanced Studies, DIAS Dunsink Observatory, Dublin D15 XR2R, Ireland
- Max-Planck-Institut f
 ür Kernphysik, P.O. Box 103980, D 69029 Heidelberg, Germany
- ⁴ Laboratoire Leprince-Ringuet, École Polytechnique, CNRS, Institut Polytechnique de Paris, F-91128 Palaiseau, France
- University of Namibia, Department of Physics, Private Bag 13301, Windhoek 10005, Namibia
- ⁶ Centre for Space Research, North-West University, Potchefstroom 2520, South Africa
- ⁷ Institut für Physik und Astronomie, Universität Potsdam, Karl-Liebknecht-Strasse 24/25, D 14476 Potsdam, Germany
- Beutsches Elektronen-Synchrotron DESY, Platanenallee 6, 15738 Zeuthen, Germany
- ⁹ Institut für Physik, Humboldt-Universität zu Berlin, Newtonstr. 15, D 12489 Berlin, Germany
- ¹⁰ LUX, Observatoire de Paris, Université PSL, CNRS, Sorbonne Université, 5 Pl. Jules Janssen, 92190 Meudon, France
- Sorbonne Université, CNRS/IN2P3, Laboratoire de Physique Nucléaire, et de Hautes Energies, LPNHE, 4 place Jussieu, 75005 Paris, France
- ¹² IRFU, CEA, Université Paris-Saclay, F-91191 Gif-sur-Yvette, France
- Friedrich-Alexander-Universität Erlangen-Nürnberg, Erlangen Centre for Astroparticle Physics, Nikolaus-Fiebiger-Str. 2, 91058 Erlangen, Germany
- ¹⁴ Instytut Fizyki Jacadrowej PAN, ul. Radzikowskiego 152, ul. Radzikowskiego 152, 31-342 Kraków, Poland
- ¹⁵ Université Paris Cité, CNRS, Astroparticule et Cosmologie, F-75013 Paris, France
- School of Physics, University of the Witwatersrand, 1 Jan Smuts Avenue, Braamfontein, Johannesburg, 2050, South Africa
- School of Physical Sciences and Centre for Astrophysics & Relativity, Dublin City University, Glasnevin, Dublin D09 W6Y4, Ireland
- ¹⁸ University of Oxford, Department of Physics, Denys Wilkinson Building, Keble Road, Oxford OX1 3RH, UK, United Kingdom
- ¹⁹ Aix Marseille Université, CNRS/IN2P3, CPPM, Marseille, France
- Laboratoire Univers et Particules de Montpellier, Université Montpellier, CNRS/IN2P3, CC 72, Place Eugène Bataillon, F-34095 Montpellier Cedex 5, France
- Université Bordeaux, CNRS, LP2I Bordeaux, UMR 5797, F-33170 Gradignan, France
- ²² School of Science, Western Sydney University, Locked Bag 1797, Penrith South DC, NSW 2751, Australia
- ²³ Landessternwarte, Universität Heidelberg, Königstuhl, D 69117 Heidelberg, Germany
- ²⁴ Institut für Astronomie und Astrophysik, Universität Tübingen, Sand 1, D 72076 Tübingen, Germany
- Universität Innsbruck, Institut für Astro- und Teilchenphysik, Technikerstraße 25, 6020 Innsbruck, Austria
- Obserwatorium Astronomiczne, Uniwersytet Jagielloński, ul. Orla 171, 30-244 Kraków, Poland
- ²⁷ Institute of Astronomy, Faculty of Physics, Astronomy and Informatics, Nicolaus Copernicus University, Grudziadzka 5, 87-100 Torun, Poland
- Nicolaus Copernicus Astronomical Center, Polish Academy of Sciences, ul. Bartycka 18, 00-716 Warsaw, Poland

- ²⁹ GRAPPA, Anton Pannekoek Institute for Astronomy, University of Amsterdam, Science Park 904, 1098 XH Amsterdam, The Netherlands
- ³⁰ Department of Physics and Astronomy, University of Manitoba, Winnipeg, MB, R3T 2N2, Canada
- School of Physical Sciences, University of Adelaide, Adelaide 5005, Australia
- 32 Yerevan Physics Institute, 2 Alikhanian Brothers St., 0036 Yerevan, Armenia
- ³³ Department of Physics, Konan University, 8-9-1 Okamoto, Higashinada, Kobe, Hyogo 658-8501, Japan
- ³⁴ Institute for Cosmic Ray Research, University of Tokyo, 5-1-5, Kashiwa-no-ha, Kashiwa, Chiba 277-8582, Japan
- 35 Kapteyn Astronomical Institute, University of Groningen, Landleven 12, 9747 AD Groningen, The Netherlands
- ³⁶ Department of Applied Physics, Faculty of Engineering, Kanagawa University, 3-27-1 Rokkakubashi, Kanagawa-ku, Yokohama, Kanagawa 221-8686, Japan

^{*}now at 29

Appendix A: Analysis details and derivation of systematics

A.1. Residual maps

Figure A.1 shows the same significance map as in Figure 1, but with the emission region covered to highlight the background normalisation. The values in the map are used to make a histogram which is used to verify that the background model describes the observations well.

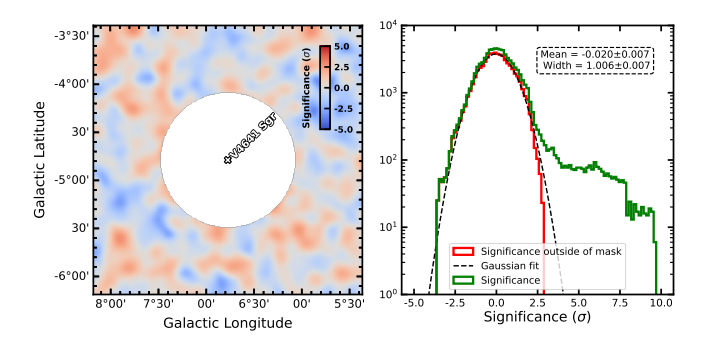


Fig. A.1. *Left:* The same significance map as in Figure 1, but with the exclusion mask covering V4641 Sgr and a colour range which focuses on the background fluctuation scales. *Right:* The distribution of the significance values outside of an exclusion mask covering V4641 Sgr (red line) and over the entire map (green line). A Gaussian function is fit to the red distribution (black line), with mean -0.020 ± 0.007 and width 1.006 ± 0.007 , close to the values of mean 0 and width 1 expected if the background is perfectly modelled.

A.2. Additional models considered

Table A.1 contains the best-fit parameters of models which were considered, but which cannot be statistically distinguished from those in Table 1. The model A_{disk} has an additional parameter η which parametrises the shape of the spatial model between a flat disk morphology (η = 0.01) and a peaked Laplace profile
(η = 1). The choice of shape has most impact on the extent of the emission for relatively high containment fractions. In the Gaussian scenario, the 68% and 95% containment radii along the major axis are (55.4 ± 6.3)d_{6.2kpc} and (88.6 ± 10.1)d_{6.2kpc} pc respectively, whereas allowing η to be free results in (59.5 ± 6.1)d_{6.2kpc} and (70.2 ± 7.2)d_{6.2kpc} pc.

Models C and D have two elliptical components with only one and no shared parameters, respectively. In both cases, the best-fit parameters are consistent with model B.

A.3. Derivation of systematics

We estimate systematic uncertainties in the model parameters with a Monte Carlo-based approach following H.E.S.S. Collaboration et al. (2023). The concept behind this approach is that there might be discrepancies between the instrument response functions (IRFs) associated to each run and the real conditions of observations, which would introduce systematic biases in the analysis results. We identify two main sources of uncertainty: mis-modelling of the background and shifts in the energy reconstruction caused by changing atmospheric conditions.

Using a Monte Carlo approach, we randomly modify the IRFs to account for the two effects mentioned above, and use these modified response functions to simulate observations following the best-fit source models. We then re-fit these pseudodataset using the original IRFs to mimic the scenario where the

IRFs do not match the recorded data. The obtained spread in the fitted model parameters then reflects their combined statistical and and systematic uncertainty. For further details on the ways the IRFs are modified and how the scale of the modifications is chosen we refer to H.E.S.S. Collaboration et al. (2023). For certain fitted parameters, such as the coordinates and position angle of the elongated Gaussian components, the distribution is not influenced by the systematic effects considered in this scheme. However, these parameters may be affected by other systematic effects neglected in the Monte Carlo approach. In particular, the source positions are subject to a systematic uncertainty of the pointing position of the H.E.S.S. telescopes, which is of the order of 10" - 20" (Gillessen 2004) and negligible compared to the statistical errors.

The same pseudo-datasets are used when calculating systematic errors for flux points. In this case, the systematic uncertainties are negligible compared to the statistical ones.

Appendix B: X-ray coverage

Figure B.1 compares the XRISM image of the V4641 Sgr region to the H.E.S.S. contours. As can be seen, the morphology of the XRISM emission does not closely follow that of the gamma rays, nor extends as much within the XRISM FoV. A dedicated analysis of the archival *Chandra* data (Suzuki et al. 2025) revealed flux levels similar to those obtained with XRISM, although with higher systematic uncertainties due to the absence of background regions outside of the gamma-ray emission.

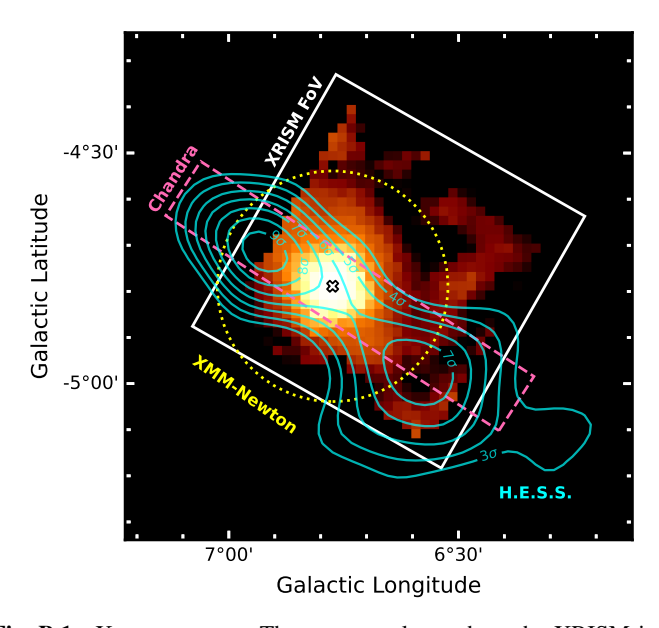


Fig. B.1. X-ray coverage. The orange colours show the XRISM image after the particle-background subtraction and vignetting correction (Figure 2c from Suzuki et al. 2025). The FoV of XRISM is denoted with a white box. The blue contours are the same as shown in black in Figure 1, outlining the H.E.S.S. emission. Existing coverage by *Chandra* and *XMM-Newton* is shown with pink dashed and yellow dotted lines, respectively.

Appendix C: Details on the estimation of the gas density

C.1. Molecular gas

 12 CO(J=1-0) measurements were obtained with the Nobeyama Radio Observatory (NRO) 45 m radio telescope between February and March 2025. An area of $0.8 \times 1.4^{\circ}$ centred at

30

10

20

25

35

Table A.1. Best-fit parameters for additional spectro-morphological models considered.

Model	ϕ_0 (10 ⁻¹³ TeV ⁻¹ cm ⁻² s ⁻¹)	Γ	E ₀ (TeV)	l (deg)	b (deg)	$\sigma_{ m major} \ ({ m deg})$	$\sigma_{ m minor} \ m (deg)$	e	θ (deg)
	single	e elliptical con	nponent v	with $\eta = 0.25 \pm 0$.	.13, $(\Delta TS_A = 2.2, A)$	$\Delta N_{dof} = 1 \rightarrow 1.$	5 <i>σ</i>)		
A_{disk}	1.60 ± 0.24	1.82 ± 0.11	2	6.718 ± 0.032	4.880 ± 0.026	0.56 ± 0.06^a	0.10 ± 0.02^a	0.983 ± 0.005	52.6 ± 2.0
		two comp	onents, sl	nared angle, (ΔTS	$S_A = 20.1, \Delta N_{dof} =$	$=6 \rightarrow 3\sigma$)			
C1	0.88 ± 0.21	1.80 ± 0.16	2	6.889 ± 0.028	-4.746 ± 0.20	0.16 ± 0.05	0.04 ± 0.02	0.961 ± 0.033	58.6 ± 4.4
C2	1.08 ± 0.29	1.96 ± 0.19	2	6.522 ± 0.042	-5.065 ± 0.036	0.18 ± 0.05	0.11 ± 0.05	0.792 ± 0.174	-
		two cor	nponents	, all free, $(\Delta TS_A =$	$= 21.8, \Delta N_{dof} = 7$	$\rightarrow 3\sigma$)			
D1	0.68 ± 0.19	1.75 ± 0.16	2	6.917 ± 0.023	-4.726 ± 0.016	0.11 ± 0.03	0.05 ± 0.02	0.894 ± 0.085	60.2 ± 9.1
D2	1.12 ± 0.25	1.95 ± 0.18	2	6.543 ± 0.03	-5.014 ± 0.026	0.17 ± 0.07	0.10 ± 0.07	0.815 ± 0.261	59.3 ± 19.7

Notes. Uncertainties are statistical only. Systematic uncertainties should be taken as of similar magnitude as those in Table 1. (a) Note that the best-fit spatial scales σ_{major} and σ_{minor} correspond to roughly 68% containment radii for $\eta = 0.25$ but 39% for the Gaussian ($\eta = 0.5$) case.

R.A.=18h19m28.8s, Dec = $25^{\circ}39$ m36s was scanned in constant declination bands. The total observation time added up to roughly 20 h. The beamwidth of the NRO 45-m telescope is 15". For each pixel covered, a velocity with respect to the local standard of rest ($V_{\rm LSR}$) spectrum with resolution $\Delta V_{\rm LSR}$ = 0.2 km s⁻¹ was obtained. The velocity coverage ranges from -150 to 150 km s⁻¹. The spatial and velocity grids have pixel sizes of 7.5" and 0.2 km s⁻¹, respectively. Further details on the data-reduction steps follow those detailed in Tsuji et al. (2025).

10

Assuming a distance of 6.2 kpc places V4641 Sgr at a galacto-centric radius $R_{\rm gal} = 2.11$ kpc (3.23 and 0.96 pc for distances of 5 and 8 kpc, respectively). At such small $R_{\rm gal}$, the Galactic rotation curve is relatively poorly constrained. We use the parametrisation provided by Sofue (2015) to transform the velocities in the measured spectra to distances because it is derived using more complete observational constraints in the $R_{\rm gal} < 4$ kpc range. We will compare the results to those obtained when using different parametrisations (Brand & Blitz 1993; Reid et al. 2019) for completeness, but note that those are derived from few or no measurements at low $R_{\rm gal}$. The distance to V4641 Sgr corresponds to $V_{\rm LSR} = 64.6$ km s⁻¹ (35 and 88 km s⁻¹ for 5 and 8 kpc, respectively).

Figure 6 shows the velocity spectrum and a velocity-integrated map of $^{12}\mathrm{CO}$ around V4641 Sgr. There is no significant signal in any range other than (I) 4 km s $^{-1}$ < V_{LSR} <10 km s $^{-1}$, (II) 26 km s $^{-1}$ < V_{LSR} <31 km s $^{-1}$ and (III) -28 km s $^{-1}$ < V_{LSR} <-24 km s $^{-1}$. None of these ranges correspond to a distance consistent with any estimates of the distance to V4641 Sgr regardless of the rotation curve used.

Velocity range (I) corresponds to a near and far distances of 1.7 ± 0.62 and 14.5 ± 0.62 kpc. The emission in that range is concentrated on a region of radius ≈0.1° around the Galactic coordinates (6.393, -5.109)°, with a second, smaller bright spot around (6.233, -5.468)°. This newly discovered molecular cloud complex shows sub-structure and is likely made up of several smaller components. Velocity range (II) corresponds to near and far distances of 4.39 \pm 0.25 and 11.80 \pm 0.25 kpc, respectively. This velocity range is closest to, although still inconsistent with, the distance to V4641 Sgr and the emission is concentrated on a small (<0.05° radius) region around Galactic coordinates (6.369, -4.859)°. Velocity range (III) is just outside of the range of allowed velocities for that line of sight and all the rotation curves considered, which means the cloud has a non-negligible proper velocity. For relatively small values of the proper velocity, the closest allowed rotation velocity requires the cloud to be either very nearby (< 100 pc) or very distant (> 15 kpc). In any case, we can confidently state that this cloud does not explain the gamma-ray emission because the emission is again concentrated on a small (<0.04° radius) region around Galactic coordinates (6.995, -4.638)°. The small size favours the large distance, to match the expected physical scales of molecular clouds of tens of pc (Heyer & Dame 2015), with 0.04° corresponding to \approx 14 pc at a distance of 20 kpc. Due to the lack of correlation with the gamma-ray emission, and the inconsistent distances, a detailed study of these clouds is outside the scope of this paper and will be tackled by a follow-up paper (Tsuji et al, in prep).

Our analysis of the dedicated NRO observations yielded no molecular cloud consistent with either the morphology of the gamma-ray emission or the distance to V4641 Sgr. We can derive an upper limit to the average density in a region comparable to the gamma-ray emission from the noise level in the CO data. On scales comparable to the smallest dimension of the gammaray emission (0.1°, 10.8 pc) the noise level across the data is $\Delta T_{MB} = 0.087$ K. We derive a 99% containment upper limit on the CO intensity (W_{CO}) as W_{CO,99%} $< 3 \times \Delta T_{MB} \times \sqrt{N_{ch}} \times \Delta V_{LSR}$, where N_{ch} is the number of velocity channels for integration (velocity range divided by resolution). We adopt a velocity range for the integration of 10 km s⁻¹, larger than the typical spreads for molecular clouds (Heyer & Dame 2015), which results in $W_{CO.99\%}$ < 0.3 K km s⁻¹. Converting from CO to a column density of hydrogen requires an assumption for the CO-to-H2 conversion factor X_{CO} . In order to take into account fact that X_{CO} depends on metallicity, which in turn depends on R_{gal}, we adopt the functional form from Arimoto et al. (1996) with the same parameters as in CTA Consortium et al. (2024). This results in a conversion factor $X_{CQ}^{R_{gal}=2.11 \text{ kpc}} = 3.5 \times 10^{19} \text{ s K}^{-1} \text{ km}^{-1} \text{ cm}^{-2}$ at the distance of V4641 Sgr, consistent with Herschel estimates (Pineda et al. 2013) for low values of $R_{\rm gal}$. We assume that the depth of the cloud is the geometrical mean of the 68% containment diameter along the major and minor axis of the gammaray emission, $l \approx 46$ pc, which yields $n_{\rm H} < 0.18 \times l_{46}^{-1}$ cm⁻³.

For consistency, we also investigate the publicly available Dame Survey maps (Dame & Thaddeus 2022). Since the angular resolution of these observations is significantly worse than that of NRO, small dim clouds might not be resolved, and in fact none of the clouds mentioned above are detected - there is no emission in a radius of 1° around V4641 Sgr (see Figure C.1, panel A).

10

20

40

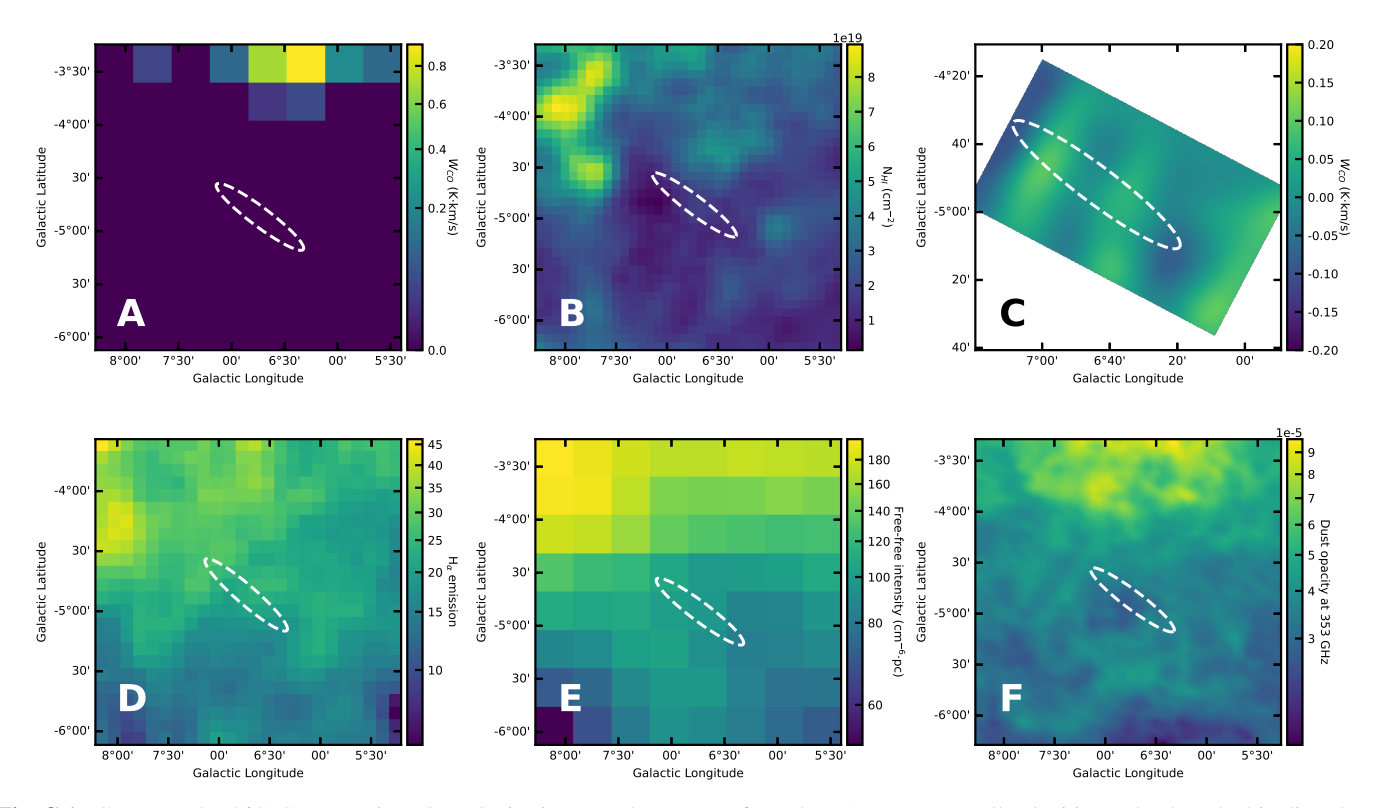


Fig. C.1. Gas around V4641 Sgr. *Panel A*: The velocity-integrated W_{CO} map from the DAME survey (all velocities). The dotted white line shows the 68% containment region of model A. *Panel B*: The same as panel A, but the map shows the hydrogen column density integrated in a range of 20 km s⁻¹ around the velocity corresponding to the position of V4641 Sgr. *Panel C*: The same as panel A, but the map shows the CO intensity (W_{CO}) from the NRO data integrated in a range of 10 km s⁻¹ around the velocity corresponding to the position of V4641 Sgr. The map has been smoothed with a 0.1° kernel to highlight the scales used to derive the density upper limit. The density upper limit was not derived using this map, but the noise level across all velocities. *Panel D*: The same as panel A, but the map shows the intensity of Hα emission integrated along the line of sight from Finkbeiner (2003). *Panel E*: Same as panel A, but the map shows the intensity of free-free emission integrated along the line of sight from Planck Collaboration et al. (2016). *Panel F*: The same as panel A, but the map shows the dust opacity integrated along the line of sight from Planck Collaboration et al. (2016).

C.2. HI, H α , free-free emission and dust

In addition to dedicated and archival CO observations, we consider the presence of atomic hydrogen through the study of 21-cm emission. We use the publicly available map from the HI4PI survey (Winkel et al. 2016) and follow the same procedure as for the CO maps, assuming optically thin gas. In the absence of lines in the relevant velocity range, we integrate the emission within a range of width 20 km s⁻¹, motivated by the mean line-width found in a decomposition of the entire HI4PI survey data (Kalberla & Haud 2018). This is a conservative choice, as this value corresponds to the warm neutral medium (WNM), which is likely hotter than the environment around V4641 Sgr – the mean line widths for the lukewarm and cold neutral media are lower by factors of more than 2 and 4, respectively (Kalberla & Haud 2018). Panel D in Figure C.1 shows the value of N_H integrated in a range of 20 km s⁻¹ around the velocity corresponding to the position of V4641 Sgr, where no neutral gas excess can be seen. We find $n_{\rm HI} \approx 0.08 \times l_{46}^{-1} {\rm cm}^{-3}$.

The HI column density map shown in panel B of Figure C.1 and density estimate obtained differs significantly from those presented in Alfaro et al. (2024). In that work, a velocity range of width 60 km s $^{-1}$ was chosen for the integration, three times larger than the average line widths of the WNM (Kalberla & Haud 2018). While the velocity range corresponds to a physical distance of almost 1 kpc (Sofue 2015), a depth of only 20 pc was adopted, resulting in a higher density estimate $(\approx 1~{\rm cm}^{-3})$ than reported here.

Furthermore, we check for the presence of ionised gas using the publicly available ${\rm H}\alpha$ map from Finkbeiner (2003). As can be seen in panel D of Figure C.1, we find no excess in the vicinity of V4641 Sgr, indicating that, in addition to no neutral or molecular gas, there is also no ionised material. There is no excess either in the Planck foreground maps⁹(Planck Collaboration et al. 2016) of integrated free-free emission (Figure C.1, panel E) or dust optical depth (Figure C.1, panel F), further confirming that V4641 Sgr sits in a low-density environment.

Appendix D: Summary of emission and acceleration scenarios considered.

Given the large uncertainties and many scenarios discussed, we have collected some of the options in Table D.1, together with the main arguments against each scenario under a fully leptonic and fully hadronic assumption. This table is not an attempt to be exhaustive, with only simple scenarios taken into account.

10

⁹https://wiki.cosmos.esa.int/planckpla2015/
index.php/CMB_and_astrophysical_component_maps#
Astrophysical_foregrounds_from_parametric_component_
separation

Table D.1. Summary of emission and acceleration scenarios considered.

		Model			Emission mechanism	echanism
Jet orientation	Jet speed	Jet length	Acceleration region	Origin of morphology	issues if leptonic	issues if hadronic
aligned with 1.o.s.	relativistic	>300 pc	near black hole	advection in jet	energy in jet cocoon very large (Equation 1) beaming should hide counter-jet (Table 1) requires weak magnetic field (B $\lesssim 3\mu$ G)	energy in jet cocoon very large beaming should hide counter-jet energy in protons very large (but benefits from beaming) proton confinement
aligned with 1.o.s.	relativistic	$<300 \text{ pc}$ lobe size $\approx 100 \text{ pc}$	in lobes/cocoon	filled lobes	energy in jet cocoon very large (Equation 1) requires weak magnetic field (B $\lesssim 3\mu G)$	energy in filled cocoon very large energy in protons very large proton confinement
aligned with 1.o.s.	relativistic	any	near black hole or further out in jet	escape from jets and diffusion into special environment	escape from jets and diffusion unclear what creates special environment into special environment unclear what determines source size requires fine-tuning diffusion $(B \lesssim 3 \mu \rm G)$	unclear what creates special environment unclear what determines source size requires fine-tuning diffusion (B \gtrsim 100 μ G) energy in protons very large proton confinement
perpendicular (hidden jet)	perpendicular (hidden jet) at least mildly relativistic $(30-70)(\sin\phi)^{-1}$ pc	$(30-70)(\sin\phi)^{-1}$ pc	near black hole	advection in jet	requires weak magnetic field (B $\lesssim 3 \mu G$) radiative cooling at acceleration site	energy in protons very large proton confinement
perpendicular (hidden jet)	perpendicular (hidden jet) — at least mildly relativistic — $(30-70)(\sin\phi)^{-1}$ pc	$(30-70)(\sin\phi)^{-1}$ pc	further out in jet	slow advection within cocoon	requires weak magnetic field (B \lesssim 3 μ G) radiative cooling at acceleration site cooling faster than transport	energy in protons very large proton confinement
perpendicular (hidden jet)	perpendicular (hidden jet) — at least mildly relativistic — $<\!(30\text{-}70)(\sin\phi)^{-1}$ pc	$<(30-70)(\sin\phi)^{-1}$ pc	further out in jet	diffusion	requires weak magnetic field (B $\lesssim 3\mu\mathrm{G})$	energy in protons very large proton confinement